

DEVELOPMENT OF A NOVEL METHOD TO OBTAIN COMPLEX SHAPED
MAGNETIC STRUCTURES FOR ADDITIVE MANUFACTURING

by

ONUR ZIRHLI

Submitted to the Graduate School of Engineering and Natural Sciences
in partial fulfillment of
the requirements for the degree of
Master of Science


Sabancı University

July 2019

DEVELOPMENT OF A NOVEL METHOD TO OBTAIN COMPLEX
SHAPED MAGNETIC STRUCTURES FOR ADDITIVE MANUFACTURING

APPROVED BY:

Assoc. Prof. Dr. Burç Mısırlıođlu
(Thesis Supervisor)




Assoc. Prof. Dr. Ozan Akdođan
(Thesis Co-Advisor)



Prof. Dr. Melih Papila



Assoc Prof. Dr. Özge Akbulut



Asst. Prof. Dr. Ali Fuat Ergenç



DATE OF APPROVAL: 18/July/2019

© Onur ZIRHLI 2019

All Rights Reserved

DEVELOPMENT OF A NOVEL METHOD TO OBTAIN COMPLEX SHAPED MAGNETIC STRUCTURES FOR ADDITIVE MANUFACTURING

ONUR ZIRHLI

Materials Science and Nano Engineering, M.Sc. Thesis, 2019

Thesis Advisor: Assoc. Prof. Dr. Burç Mısırlıoğlu

Keywords: additive manufacturing, 3d printing, hard magnet, magnetism, rare-earth free magnet, pulse magnetizer, ball milling, nitridation

ABSTRACT

Hard magnetic materials do play a critical role in numerous industrial areas relates with magnetic tapes, hard drive units, speaker drivers, biomedical measurement devices, electric motors, hybrid cars, wind turbines. Since these areas include large scale manufacturing, size and cost of the magnetic material have a direct effect on it. Magnetic energy intensity and availability of magnetic material are the main characteristics that concern size and cost-effectiveness.

Today, neodymium iron boron (NdFeB), aluminum nickel cobalt (Alnico), and ferrite are mostly used as magnetic materials. NdFeB is the most significant one among them because of its magnetic energy density. Nowadays, the world is experiencing a rare-earth material crisis. Moreover, because of its fragile nature, it is tough to make custom shaped / CNC milled NdFeB magnets, especially for prototyping. These are the main reasons that industry is in search of new, rare-earth free magnetic materials. A metastable iron nitride phase, $Fe_{16}N_2$ shows promising magnetic properties in literature and become prominent as a possible alternative to NdFeB.

In this study, we aimed to propose a solution to aforementioned problems by finding a way to synthesize $Fe_{16}N_2$ particles by using ball-milled iron micro/nanoparticles and trying to utilize it with additive manufacturing method. Furthermore, we expected to increase anisotropy, and the magnetic energy density of printed material by manipulating it with a pulse magnetizer circuit. Considering the time consumption of the configuration and optimization of the oven system, we tried to prepare 3d printing system, pulse magnetizer system simultaneously. Therefore $Fe_{16}N_2$ was not used in these systems, instead, we used ball milled NdFeB and iron flakes to show proof of concept. Prepared $Fe_{16}N_2$ particles are characterized by using XRD and SEM analysis.

EKLEMELİ İMALAT YÖNTEMİYLE KULLANILABİLECEK KOMPLEKS FORMDAKİ MANYETİK YAPILARIN ELDE EDİLMESİ İÇİN ÖZGÜN METOD GELİŞTİRİLMESİ

ONUR ZIRHLI

Malzeme Bilimi ve Nano Mühendislik, Yüksek Lisans Tezi, 2019

Tez Danışmanı: Doç. Dr. Burç Mısırlıoğlu

Anahtar Kelimeler: eklemeli imalat, kalıcı mıknatıs, manyetizma, 3 boyutlu yazıcı, nadir toprak elementleri içermeyen mıknatıs, bilyeli öğütme, darbeli mıknatıslama

ÖZET

Kalıcı mıknatıslar yakın geçmişten günümüze kadar manyetik teypler, sabit disk sürücüler, ses sürücüler, biyomedikal ölçümleme araçları, elektrik motorları, hibrit arabalar, rüzgâr türbinleri gibi birçok alanda kritik bir yer kaplamaktadır. Dolayısıyla kullanılan kalıcı mıknatısın boyutu ve maliyeti, bu sektörler için üretilen ürünleri doğrudan etkilemektedir. Boyutunu belirleyen en önemli faktör mıknatısın manyetik enerji yoğunluğu, maliyeti belirleyen ise kullanılan malzemeye ulaşım ve malzemenin işlenmesi konusundaki zorluklardır.

Günümüzde mıknatıs olarak en çok kullanılan malzemeler birkaçı neodimiyum demir boron (NdFeB), alüminyum nikel kolbalt (Alnico) ve ferrit olarak göze çarpmaktadır. Bunların arasından NdFeB yüksek manyetik enerji yoğunluğu ile sıyırılmaktadır. Ancak 2000'li yıllarda öne çıkmaya başlayan, neodimiyum gibi nadir toprak elementlerini elde edilmesindeki sıkıntılar sebebi ve NdFeB malzemesinin kırılma yapısının sonucu numerik kontrol metotları ile işlenmesinin zorlu olması ilgili sektörleri yeni manyetik malzemeler konusunda bir arayışa itmiştir. Yarı kararlı bir demir nitrür fazı olan $Fe_{16}N_2$, gösterdiği manyetik özellikler sebebiyle son dönemde bu arayışa bir çare olma potansiyeli gösteren malzemelerden biridir.

Bu tezin konusu olarak 3 farklı kolda araştırma yapılarak bahsedilen sorunlar için bir çözüm metodu geliştirilmeye çalışılmıştır. Birinci aşama olarak bilyeli öğütme ile elde edilmiş demir mikro-nano parçacıkları ile amonyak kullanılarak tüp fırında tavlanmış ve sonucunda elde edilen ürün XRD ve SEM analizleri ile incelenmiş, çıkan sonuçlar $Fe_{16}N_2$ fazının simülasyon sonucu elde edilmiş XRD verisi ile uyumluluk göstermiştir. Tezin konusu olan diğer konular bu parçacıkların üç boyutlu yazıcı ile basılmasına olanak

sağlamak, manyetik alan darbesi ile basılan yapının eş yönsüzlüğünü ve manyetik enerjisini arttırmak yer almaktadır. Ancak nitrürleme sisteminin kurulması ve optimizasyonu esnasında bu konularda geri kalmamak için, kavramların tutarlılığını kanıtlama amacı ile ve sistemin $Fe_{16}N_2$ fazı elde edilmeden önce hazır olması adına manyetik alan darbesi devresi hazırlanmış ve bilyeli öğütme sonucu oluşan demir ve NdFeB parçacıklar ile üç boyutlu baskı denemeleri yapılmıştır. İki parçacık ile yapılan baskı denemeleri başarılı olmuştur, dolayısıyla elde edilen $Fe_{16}N_2$ parçacıklarının da bu yöntemle basılması konusunda sorun yaşanmaması beklenmektedir.

*To my loving family for their infinite support,
and friends for their companionship*

ACKNOWLEDGEMENTS

I would like to express my gratitude to my thesis co-advisor and principal instructor of this project, Ozan Akdoğan. His driven nature and instructions helped me out throughout this era. I would like to express my gratitude to my thesis advisor and advisor of this project, Burç Mısırlıoğlu, for his advisory skills and support that helped us during the project.

Special thanks and gratitude to my jury members. I am sure I tested their patience and bearing from time to time. Melih Papila, never spared his support and mental reinforcement to me during my master's period. Özge Akbulut, supported, advised and enlightened me through my undergrad and grad life; and a remark for our published work, BRALL. And sincere thanks to Ali Fuat Ergenç for helping me with the electronics part of the project and accepting to be in my jury.

Another special set of thanks to Canhan Şen, Omid Moradi and Ertunga Eyüpoğlu, a.k.a. Yeeshkul! crew. They never spared their support, broaden my musical horizon, brought me back to balance when I was nervous, shown me ying and yang, another remark to our joyful moments during our radio sessions. Emre Burak Boz, my partial roommate, thank you for bailing me out on Robert Plant concert. I'll be their sweet&sour, hopefully mostly sweet.

Thanks;

To my beloved, former labmates Yelda Yorulmaz and Farzin Javanshour, may the force be with them.

To Deniz Anıl and Murat Tansan companion in fortune and misfortune.

To Onur Özensoy for the visionary brainstorming and intellectual supplements.

To Can Akaoğlu, as a labmate and polymer ink specialist.

To my colleagues, Aysu Yurduşen, İpek Bilge, Kaan Bilge, Deniz Köken, Semih Pehlivan, Ayşe Durmuş, Barış Kırıl, Melih Can Taşdelen, Gökşin Liu, Tuğçe Akkaş, Sezin Sayın, Farzin Asghari, Billur Seviniş, Ekin Berksun, İlayda Berkaş, Can Çalışkan, Senem Seven, Utku Seven, Buket Taş, Erdinç Taş, Adnan Taşdemir, Melike Barak for making week days bearable (and gossip support).

To my labmates Berkin Gürel, Melike Önder and Yazan Odeh

To Team Bio, Cevriye Pamukcu, Elif Çelik, Didem.

To my Deutsche Schule Istanbul crew.

To anyone who I might forgot.

To my family.

And heartfelt gratitude is going to my mom, Ilkay Nergiz Onur, for her boundless, unconditional support and love.

... This work was supported by TUBITAK project: 217M322

TABLE OF CONTENTS

Abstract.....	iv
Özet.....	v
Acknowledgements.....	viii
Table of Contents.....	x
List of Figures.....	xii
List of Tables.....	xiv
List of Abbreviations.....	xv
1. Introduction.....	1
1.1. Theoretical Background.....	3
1.1.1. Origin of magnetism and ferromagnetism.....	3
1.1.2. Hysteresis Loops.....	4
1.1.3. Magnetic Anisotropy.....	5
1.1.4. Fe-N martensite Fe_{16}N_2	6
1.2. Novelty.....	8
2. Experimental Procedure.....	9
2.1. Manufacturing Methods.....	9
2.1.1. Synthesis of Iron Flakes and nano-particles with Ball Milling.....	9
2.1.2. Tube Furnace Nitridation.....	12
2.1.3. Ink Preparation for 3D-Printing.....	15
2.2. Characterization.....	18
2.2.1. Vibrating Sample Magnetometer.....	18
2.2.2. X-Ray Diffraction.....	19
2.2.3. Scanning Electron Microscopy.....	20
3. Results and discussion.....	23
3.1. Particle Size Analysis.....	23
3.1.1. DLS Results.....	23

3.1.2. SEM Analysis of Flakes	26
3.2. Phase Analysis	28
3.2.1. Simulated XRD Graphs	28
3.2.2. XRD Results and Phase Composition	31
3.2.2.1. Nitridation Time and Temperature dependency of Fe ₁₆ N ₂ composition 33	
3.2.2.2. Stability of Fe ₁₆ N ₂ flakes under vacuum and air exposure	35
3.2.2.3. Analysis of the effect of the stirring	36
3.3. Magnetic Properties	37
3.3.1. VSM Results	37
3.4. Printed Iron Structure	40
Bibliography	45

LIST OF FIGURES

Figure 1 Hysteresis Loop (Jiles 1991).....	5
Figure 2 Iron-Nitrogen phase diagram (Dirba 2017)	6
Figure 3 Interstitial sites in FCC and BCC iron (Jack and Jack 1973).....	7
Figure 4 Illustration of ball milling surfactant assistance	10
Figure 5 MTI Corporation SFM-1 Planetary Ball Mill	11
Figure 6 Tube Furnace used in the nitridation process.....	13
Figure 7 Gas flow controllers of the nitridation system	14
Figure 8 Illustration of steps of the nitridation process	15
Figure 9 Copolymer and iron flake suspension mixed with a mechanical stirrer	17
Figure 10 Representation of a VSM system.....	18
Figure 11 Bruker D2 Phaser	19
Figure 12 Bragg's law in action	20
Figure 13 Leo SUPRA 35VP FEG-SEM	21
Figure 14 The teardrop shape of the interaction volume.....	22
Figure 15 Particle Size vs Time graph	24
Figure 16 Size vs Intensity distribution of 30 rpm speed	24
Figure 17 Size vs Intensity distribution of 50 rpm speed	25
Figure 18 (a) shape and distribution of the Iron flakes, (b) after nitridation process (c)thickness of the iron flakes,.....	27
Figure 19 α -Fe simulated XRD peaks	29
Figure 20 $Fe_{16}N_2$ simulated XRD peaks.....	29
Figure 21 Fe_2N simulated XRD peaks	30
Figure 22 Fe_3N simulated XRD peaks	30
Figure 23 Comparison of XRD measurement of synthesized $Fe_{16}N_2$ flakes with simulated $Fe_{16}N_2$ XRD peaks.....	31
Figure 24 XRD comparison of Fe flake and Fe powder	32
Figure 25 Rietveld analysis of $Fe_{16}N_2$ sample with highest transition (190°C 16h) through PowderCell	34
Figure 26 XRD comparison of fresh and air exposed $Fe_{16}N_2$ flakes.....	36
Figure 27 VSM measurement of $Fe_{16}N_2$ flake (nitridation for 40 hours at 170°C)	38
Figure 28 Comparison of $Fe_{16}N_2$ flake with Fe flake.....	38

Figure 29 Enlarged VSM measurement data to show coercivity difference of Fe ₁₆ N ₂ and Fe flakes	39
Figure 30 3D-printed iron flake sample	40
Figure 31 SEM image of iron flakes distribution in polymer	41
Figure 32 SEM image of the cross section of 3D printed iron flakes after sintering	42

LIST OF TABLES

Table 1 Size and quantity of the hardened steel balls used during high energy ball milling process	12
Table 2 Composition results of the PowderCell analysis for 16h nitridation with varying temperatures.....	33
Table 3 Fe ₁₆ N ₂ phase percentage calculations with PowderCell, an overview of the research	34
Table 4 PowderCell analysis of the vacuum stored Fe ₁₆ N ₂ (180 °C 16h)	35
Table 5 PowderCell analysis of the vacuum stored Fe ₁₆ N ₂ (190 °C 16h).....	35
Table 6 PowderCell analysis of the stirred samples	37

LIST OF ABBREVIATIONS

NdFeB:	Neodymium Iron Boron
BC:	Before Christ
AD:	Anno Domini
Alnico:	Aluminum nickel cobalt
H_c :	Coercive field
M_s :	Saturation magnetization
ORR:	Oxygen Reduction Reaction
HRR:	Hydrogen Reduction Reaction
NP:	Nanoparticle
MOKE:	Magneto-optic kerr effect
XRD:	X-Ray Diffraction
SEM:	Scanning Electron Microscope
(S)TEM:	(Scanning) Transmission Electron Microscope
VSM:	Vibrating Sample Magnetometer
UV:	Ultraviolet
PBS:	Phosphate-buffered saline

1. INTRODUCTION

The history of the interaction between humankind and the magnetism goes back to the pre-common era. Earliest reference known in the records belongs to Greek philosophers of 6th century BC (Mills 2004). They observed some interaction with metallic iron which they cannot explain. Just like every other phenomenon that humankind discovers, we managed to manipulate this interaction of magnetic materials with a magnetic field. That journey begins with utilizing lodestone as a compass needle by Chinese mariners back in AD 1080 (Mills 2004). Another milestone in the history of magnetism could be considered as, centuries later, the discovery of electromagnetism by Oersted in 1819 (Byrneumledu 2012). Oersted observed that the behavior of the compass needle changes when a current-carrying wire was placed nearby (Weiss 2000). This discovery opens another realm of possibilities for the world of magnetism. Interactions with electromagnetic effects bring new capabilities to the field. In today's world our power over magnetism yields products such as magnetic tapes, hard drive units, speaker drivers, biomedical measurement devices, electric motors, hybrid cars and wind turbines (Jaćimović et al. 2017; Dirba 2017; Edwards et al. 2008; Kartikowati 2018; Abdelrahman and Youssef 2017; Mornet et al. 2004). As we use magnetic mass storage devices dominantly in every field of human development, it is evident how prominent the effect of the phenomenon is on our daily life (Jiles 1991).

Another important role of magnetic materials would be its impact on green energy. One of the modern era concerns is global warming and its proliferation by society (Dirba 2017). This increases the significance of the green energy producing methods. The obvious initial step would be increasing the efficiency of green energy sources such as wind turbines and hydroelectric dams, which is highly dependent on the capability of hard magnets. Historical evolution of the magnet industry brought NdFeB magnets to increase the abilities of the means of energy production (Ma et al. 2002). NdFeB magnets show prominent properties by performing high magnetic energy, near-net-shape formability and environmental stability (Brown, Ma, and Chen 2002). Although NdFeB increases magnetic energy for energy production significantly, it also has its drawbacks. It is a rare-

earth material, which means it is not easily and globally available (Du and Graedel 2011). There are regulations on NdFeB mining operations because of possible harm to the environment (Alonso et al. 2012; Gwenzi et al. 2018). China does not follow the same regulations and as a result, becomes the leading supplier of NdFeB (Haque et al. 2014). This emerges the need for an alternative magnetic material with high magnetic energy and free from rare-earth elements (Feng et al. 2017).

Therefore, the main aim of this work, under the influence of the aforementioned findings, is to provide an alternative magnetic material for the industry and to utilize it. This research does focus on synthesizing Fe_{16}N_2 , which shows promising magnetic properties (Ji et al. 2013; Y. Sugita et al. 1991; Sakuma 2002; Kim and Takahashi 1972), as an alternative to NdFeB. Fe_{16}N_2 is formed with iron and nitrogen elements which satisfy the drawbacks of NdFeB. Fe_{16}N_2 is a metastable phase and starts to decompose at 222 °C (Takagi et al. 2014; Widenmeyer, Hansen, and Niewa 2013).

As the chemical formula of Fe_{16}N_2 shows, proposed magnetic material contains two elements that widely available in the world, nitrogen, and iron. Iron is one of the main elements that constitute earth crust which makes it one of the easiest to find in nature. Iron is also environment-friendly by being efficiently recyclable (Pepperhoff and Acet 2001). Ammonia is being used extensively in the food industry as fertilizer and farm fields (Bell, Towler, and Fan 2011). As a result, ammonia becomes one of the most highly produced chemicals in the world (Williams and Pattabathula 2013). This abundancy of iron and nitrogen makes any compound, that consists of both, inherently alternative to rare-earth magnets. When abundancy combined with expected magnetic properties, Fe_{16}N_2 becomes a promising candidate for the future of the permanent magnets (Ogawa et al. 2013). Early reports show that magnetic moment of Fe_{16}N_2 can reach 3.0 μ_B to 3.5 μ_B per iron atom (Kim and Takahashi 1972; Y. Sugita et al. 1991; Yutaka Sugita et al. 1996). Magnetic saturation value M_s varies from 2.5 T to 3 T (Y. Sugita et al. 1991) and magnetic anisotropy energy (MAE) values are between 0.44 MJ/m³ to 2 MJ/m³ (Kita et al. 2017; Takahashi et al. 1999). A compelling new composition would affect our daily life by overcoming the dependency of the energy industry to rare-earth magnets. Many consumer electronics do benefit from magnets as well. Considering the scale of magnets used in consumer electronics, magnets used in the energy industry are considerably larger. Compared by the weight, in consumer electronics magnet usage would be around 1 g,

though in electric vehicles the weight gets over 1kg and in large-scaled energy generators such as wind turbines it weights up to 2000 kg (Yang et al. 2017).

To synthesize Fe_{16}N_2 permanent magnet, a low-temperature shaping method is required. Thus, additive manufacturing method is selected. Besides being favorable for our compound, additive manufacturing could bring other advantages compared to the traditional manufacturing methods. Common methods of custom magnet production forces production band to mass production because of the high expenditures of special tooling and shape of the magnet limited with the injection molding, hot-pressing abilities (Ibeh 2018). Additive manufacturing also increases production efficiency by decreasing expensive rare-earth element waste and increasing magnetic properties with net-shape production ability, according to recent research (Popov et al. 2018). To achieve a polymer-based printing method, a grafted copolymer is used (Hodaei et al. 2018). Synthesis and printing of Fe_{16}N_2 was the main objective of this research. The 3D-printing system was ready before Fe_{16}N_2 synthesis achieved, hence instead of Fe_{16}N_2 , iron and NdFeB flakes are used to prepare polymer mixture and print it to show proof of concept. An in-house designed pulse magnetizer is prototyped to magnetize printed samples after the sintering process.

1.1. Theoretical Background

1.1.1. Origin of magnetism and ferromagnetism

Crystal structure of a material and electronic configuration dictates the magnetic properties. Electrons exhibit two different kinds of motion. They are called orbital motion and spin motion. Spin and orbital motion, each produces a magnetic moment. The magnetic moment of the atom can be defined as the sum of the magnetic moments caused by the spin and orbital motion. Different types of magnetism are oriented by the exchange interactions of atoms and diversity on the arrangements of atoms. Ferromagnetism,

diamagnetism, antiferromagnetism, paramagnetism and ferrimagnetism can be listed as types of magnetism.

Magnetic properties highly depend on the uncoupled electron number in orbitals. Pauli principle dictates how electrons will fill orbitals. When orbitals are filled, magnetic moments of electrons cancel each other. Orbitals being half filled means it can be oriented by the external field, and it can turn into a magnet. According to Hund's rule, the ferromagnetic property will drive by the quantum numbers for ground states of the atom. 3d transition metals have an outer shell 3d orbitals, with uncoupled electrons, and outer shell with 4f electrons are called 4f rare-earth elements. A convenient way to label magnetic properties is measuring the reaction under an extrinsic magnetic field.

1.1.2. Hysteresis Loops

Magnetic moment vs magnetic field graph is also called a hysteresis loop. The hysteresis loop is used to show the magnetization behavior of a ferromagnetic material.

The hysteresis loop is measured experimentally. It measures the materials response and retentivity against changing magnetic field. The system applies an increasing magnetic field (H) through an electromagnet to the sample to be reviewed. While the magnetic field increases, a sensor reads a magnetic moment of the sample in each magnetic field increment. The magnetic field keeps rising until the magnetic moment of the sample reaches saturation so that the magnetic moment limit can be observed. To be able to measure coercivity, magnetic field decreases and when it arrives at zero, the polarity of the field would change. However, the magnetic moment does not decrease with the magnetic field, as can be seen in **Figure 1**. Aligned magnetic domains resist against the decreasing magnetic field. As the magnetic field reaches to point zero material with high coercivity keeps its magnetic moment. Reversed magnetic field applies in order to see when will the sample give up and loose its magnetic domain alignment. Applied magnetic field goes to other direction in order to draw out the magnetic saturation point on the other direction. To be able to draw whole loop, magnetic field increase until the

positive saturation point, then decrease until the negative saturation points and as lastly increases to the positive magnetic saturation point again.

Materials with higher coercivity performs a wider hysteresis loop and called hard magnet, lower coercivity performs thinner hysteresis loop and called soft magnetic.

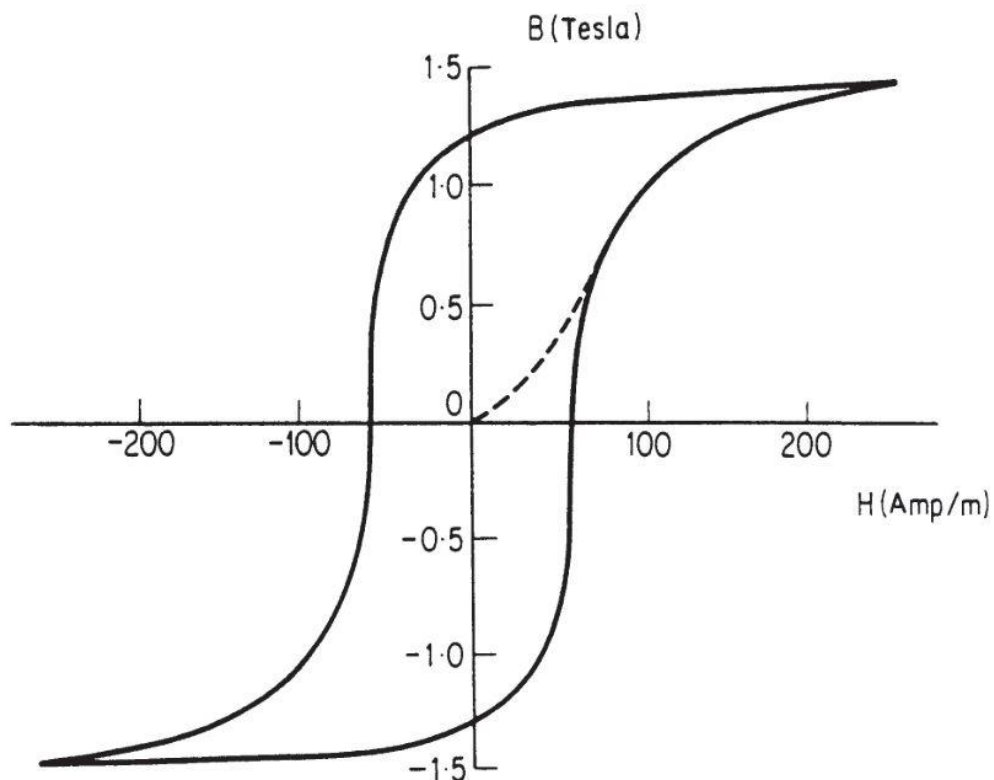


Figure 1 Hysteresis Loop (Jiles 1991)

1.1.3. Magnetic Anisotropy

Ferromagnets consist of subdivisions called domains. These domains are spontaneously magnetized. At saturation point they reach a stability point; however every domain has a different direction of magnetization. Magnetic anisotropy is magnetic properties dependence to a preferred direction. Magnetocrystalline anisotropy depends on

the crystal structure, shape anisotropy depends on the grain shape, and stress anisotropy depends on applied or residual stress.

1.1.4. Fe-N martensite α'' -Fe₁₆N₂

The constitution of ordered martensite α'' -Fe₁₆N₂ compound upon nitriding of iron by NH₃ or other nitriding agents relies on well-established surface hardening techniques of iron and steel industry. The Fe-N phase diagram shows similarities to the Fe-C diagram (Dirba 2017). Interstitial N atoms incorporate into available empty sites into Fe lattice, assuming local equilibrium phases ferrite (BCC-space group Im3m), which is stable below 1192 K with atomic nitrogen solubility 0.3 %. Austenite (FCC-space group Fm3m) with atomic nitrogen solubility 10.3 %. Apart from main phases, FCC structured nitride phases Fe₄N or γ' with %20 N solubility and HCP type Fe₂-3N or ϵ , a nitride phase with a close-packed hexagonal structure, with atomic nitrogen solubility between 15 and 33%. Fe₁₆N₂ is a non-equilibrium phase with ordered martensite structure with body-centered tetragonal as seen in **Figure 2**.

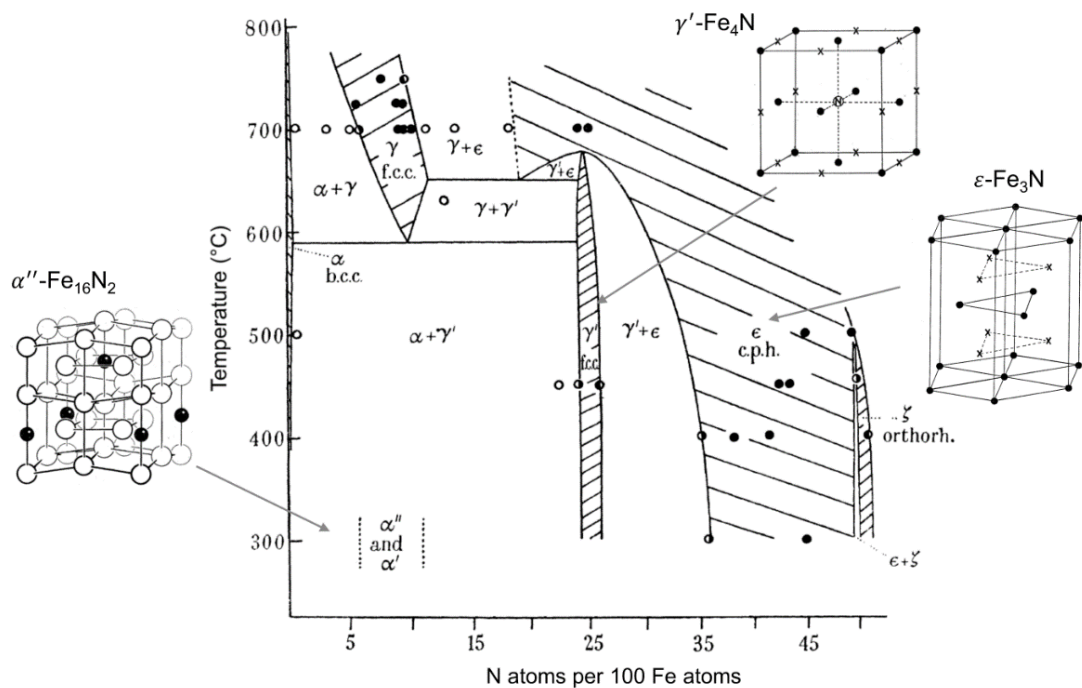


Figure 2 Iron-Nitrogen phase diagram (Dirba 2017)

Depending on the size of the interstitial N atom, Fe lattice transforms into lower symmetry crystal due to local strain. The reason lying behind the cubic-tetragonal transformation is the occupation of octahedral sites by interstitial N atom and change c/a ratio in both BCC and FCC structures. In other words, octahedral sites in BCC lattice anisotropically are distorted due to limited solubility of the N atom.

Tempering, as a well-established process step for disorder-order transformation for martensitic steels, is also a viable procedure for disordered α' -Fe₈N to ordered α'' -Fe₁₆N₂ around 370-420 K range (Moradifar 2015). α'' -Fe₁₆N₂ is composed of distorted eight α -Fe lattices with a body-centered tetragonal structure (space group I4/mmm). Nitrogen atoms are located at (0,0,0) and ($\frac{1}{2}$, $\frac{1}{2}$, $\frac{1}{2}$). N:Fe=0.125:0.875 composition, Another method proposes α'' -Fe₁₆N₂ nanoparticle synthesis indirectly following the route $\gamma \rightarrow \alpha' \rightarrow \alpha''$ (Gölden 2018).

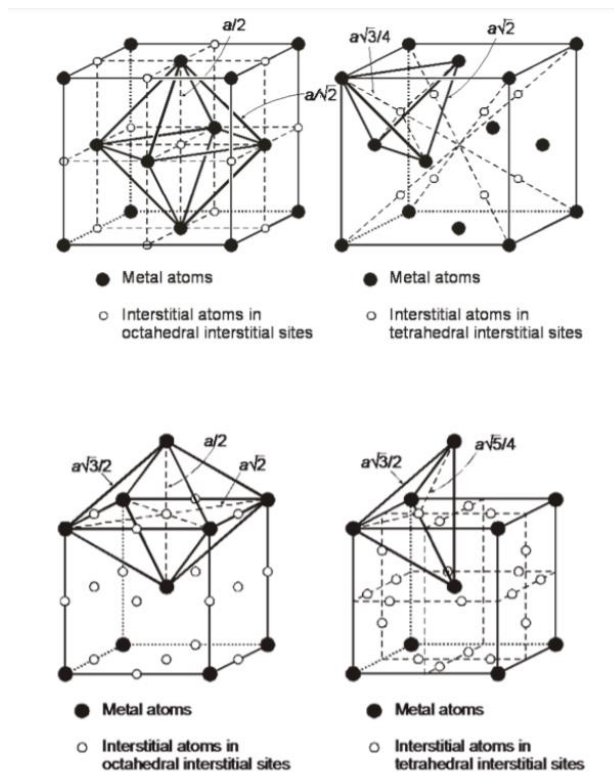


Figure 3 Interstitial sites in FCC and BCC iron (Jack and Jack 1973)

1.2. Novelty

To the best of our knowledge, research on Fe_{16}N_2 was focused on thin films, nanoparticles and irregularly shaped powders (Kim and Takahashi 1972; Y. Sugita et al. 1991; Weber et al. 1996; Takahashi et al. 1993; Ji et al. 2013; Abdellateef et al. 2003). In this study pure Iron flakes, which is naturally anisotropic due to its shape thus has better advantages in permanent magnets, has been used and 3D printing has been utilized to synthesize this alloy in permanent magnet form for the first time.

2. EXPERIMENTAL PROCEDURE

2.1. Manufacturing Methods

2.1.1. Synthesis of Iron Flakes and nano-particles with Ball Milling

Ball milling is a mechanical grinding method that is being used for mechanical alloying experiments, material mixing, and size reduction of ceramic, mineral and metallic powders(Suryanarayana 2001). In this research, the ball milling method is used to grind micron-sized iron powder and produce 100nm - 200nm thickness flake shaped iron particles.

Ball milling method uses high energy collisions of the balls by encapsulating them and powder material to be processed in a holder and constantly rotating the system. Hence this method requires powder sized materials, ceramic or steel balls to crush the powder, a vial to keep powders and balls intact and a mechanical structure to rotate holder with the required energy. As a result, balls crush the powdered material, causing a reduction in size by breaking them down and change their structures. This structure change could mean amorphization, changing shape or composition. A laboratory-scale planetary ball mill with 4 vials, MTI Corporation SFM-1 can be seen in **Figure 5**, is used in this research to prepare iron flakes to be used in the nitridation system. Planetary ball mill benefits from the planet like motions of the vials. Vials rotate around both their own axes and center of the system.

Stainless steel balls and vials have been used in our experimental setup. To decide rotation speed and experiment time, different flake batches with 30 rpm, 40 rpm and 50 rpm, milled for 4 to 24 hours. Powders milled for 24 hours with 50 rpm speed was used for further experiments.

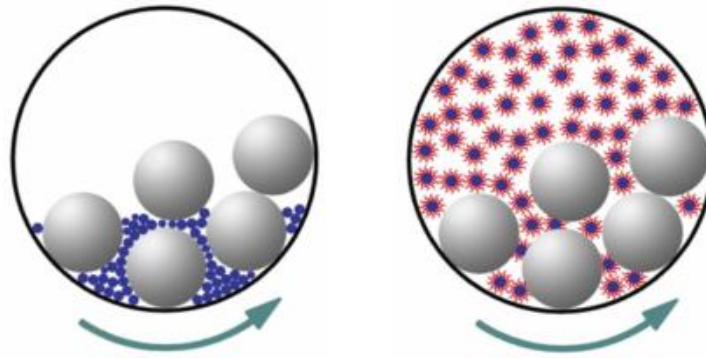


Figure 4 Illustration of ball milling surfactant assistance

The mechanical energy that causes steel balls to break powder into smaller pieces depends on the ratio of the weight of the steel balls to the weight of the powder to be milled. The setup of the previous researches varies from 1:1 weight ratio to 220:1 weight ratio (Kis-Varga and Beke 1996; Chin and Perng 1996). In our experimental setup, 10:1 ball to powder ratio is used to achieve aimed size reduction. Another limitation here is the vial size to decide how much powder and balls to be used. Eleven grams of 10-micron sized iron powder (Merck 103815.1000) and 127 grams of steel balls with various sizes held into steel vials. **Table 1** shows the related ball sizes.

Another variable in the ball milling method is the usage of dispersant. There is dry ball milling without using any liquid dispersant and wet ball milling to be able to produce well-dispersed particles. Dry ball milling could cause crushed particles to weld together by cold welding (Jiang et al. 2016). Welding causes an increase in surface and particle size. This hinders the ball mill system to achieve smaller sized particles. Since smaller particle size could be beneficial for the following nitridation process wet ball milling method is chosen. The literature also shows us in order to prevent welding, in addition to dispersant, a surface-active agent (surfactant) could be used (Nilay G. Akdogan, Hadjipanayis, and Sellmyer 2010). Heptane is chosen as the dispersant material and oleic acid is chosen as the surfactant, based on the previous research, to be able to produce highly dispersed, nano-scaled iron flakes by using micron-sized Iron particles as raw material (Nilay Gunduz Akdogan 2012).

To summarize the first step of the experimental setup, a planetary ball mill system with 4 vial capacity is used with 2 vials. Stainless steel is chosen as the ball and vial

material. The dispersant is selected as Heptane and 1.5 ml oleic acid is used as the surfactant. Ball to powder ratio is set as approximately 10:1 with 11 grams of powder and 127 grams of steel balls. Speed and time are selected as 50 rpm for 24 hours.



Figure 5 MTI Corporation SFM-1 Planetary Ball Mill

After ball milling process synthesized iron flakes were dispersed in heptane and coated with oleic acid. Hence it requires a cleaning process before nitridation. In order to clean iron flakes, ethanol is being used. Half of the 50 ml falcon tube filled with flake mixture and the other half filled with ethanol. Then falcon tube is centrifuged at 4500 rpm to separate iron flakes and nanoparticles from heptane/ethanol solution. Heptane/ethanol solution is spilled out and this process is repeated three times to make sure particles are cleaned. This process ends up by acquiring cleaned iron flakes combined with iron nanoparticles. Detailed explanation about the size of the particles will be discussed in the third chapter.

Table 1 Size and quantity of the hardened steel balls used during high energy ball milling process

Size (diameter)	Quantity
13,48 mm	2
11,85 mm	4
9,95 mm	6
7,91 mm	19
4,83 mm	34

2.1.2. Tube Furnace Nitridation

After the ball milling process, the surface area of iron powder increases and since this phase transformation is diffusion controlled, Fe_{16}N_2 transformation is expected to be more favorable. Previous research studies focused on thin film deposition and nano-particle synthesis of Fe_{16}N_2 by reducing iron-oxide nano-particles to α -Fe and applying the nitridation process. Since our precursor material is already α -Fe, early oven recipe did not include a reduction process. Initial oven procedure includes placing iron flakes into crucibles made from molybdenum which is placed into the center of the tube furnace.

Instead of using crucibles made from alumina, we made molybdenum crucibles in order to prevent any contamination from the crucible itself. Molybdenum is a convenient material to be used as a crucible, since it has a high melting point at 2610 °C and is resistive against corrosion.

The tube furnace setup, that can be seen in **Figure 6** and **Figure 7**, aims to achieve Fe_{16}N_2 from α -Fe by low temperature nitridation. Conducted experiments could be examined in three different parts.

In the first part, the tube is purged with 99% Argon gas after placing samples into the tube furnace. Low temperature nitridation experiments are conducted under 50 scc/m 99% pure NH_3 gas flow with varying time parameter up to 48 hours.

As the second part of the low temperature nitridation experiments, another parameter is introduced to the system, hydrogen reduction. The reason for the addition of

this step is to prevent any superficial oxidation layer and to remove any oleic acid residue. Now the experimental scheme involves hydrogen reduction of the iron flakes at 400 °C, cooling down to nitridation temperature under Argon gas flow, and NH₃ gas flow at nitridation temperature with variable time parameter respectively. NH₃ gas flow is fixed to 100 scc/m. Gas flow control setup can be seen in **Figure 7**. Time parameter varies between 16 hours to 160 hours. Nitridation temperature varies between 150 °C to 200 °C.



Figure 6 Tube Furnace used in the nitridation process

In the third phase of the procedure, another step is introduced. This time mixing is introduced to the system. While Fe₁₆N₂ emerges, the sample is mixed every 16 hours, to prevent any structural difference between the top and the bottom of the sample. At each mixing step certain amount of sample is collected for XRD measurements.

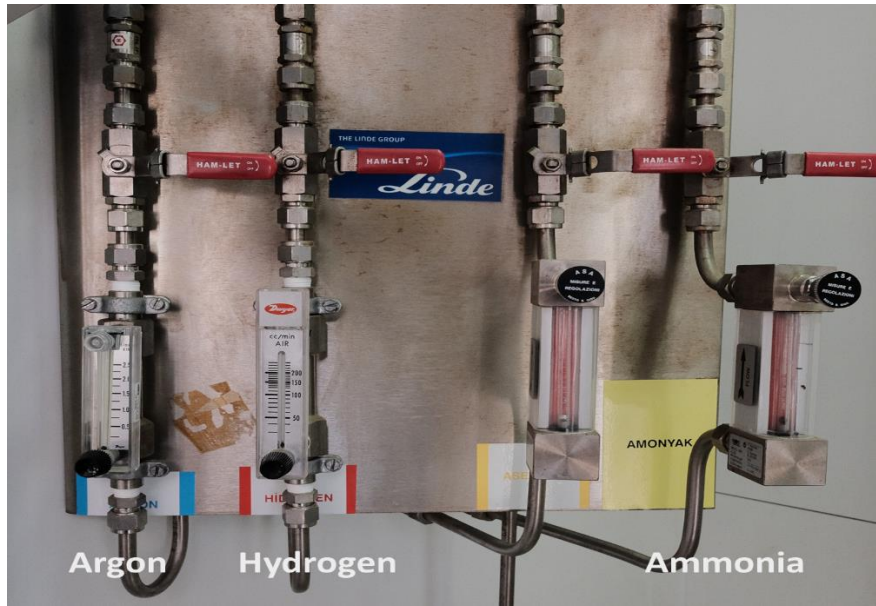


Figure 7 Gas flow controllers of the nitridation system

In all experiments, Exhaust NH_3 gas flow is neutralized with the phosphate saline buffer solution (PBS). In order to prepare 1 liter stock of 10 times concentrated (10x) PBS required materials are as the following;

- 2 grams KCl
- 80 grams NaCl
- 14,4 grams $\text{Na}_2\text{HPO}_4 \cdot 2\text{H}_2\text{O}$
- 2,4 grams KH_2PO_4
- 0,8 liters of distilled water

These materials should be mixed overnight with a magnetic stirrer. After mixing 0,2 liters of water should be incorporated. In the end, 1 liter of 10x PBS is collected. The buffer should be diluted with 9:1 water to PBS ratio to be used as exhaust neutralizer(Dulbecco 1954).

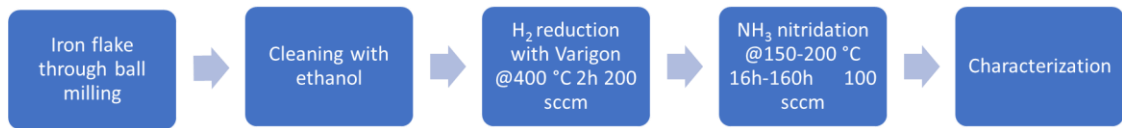


Figure 8 Illustration of steps of the nitridation process

2.1.3. Ink Preparation for 3D-Printing

Fe_{16}N_2 is a metastable phase, where it is not possible to maintain it above 222 °C. Temperature dependent metastability limits the possibilities to shape and functionalize Fe_{16}N_2 powders. Low temperature 3D-printing appears favorable to keep Fe_{16}N_2 phase stable while shaping it. Yet another advantage of additive manufacturing is producing complex shaped 3D-structures of permanent magnets. Ability to produce custom shaped magnetic structures brings increasing energy efficiency of current electro-mechanical systems that depends on magnetic materials (Gutfleisch et al. 2011). A polymer-based 3D-printing method selected to be able to shape our samples at low temperature. Experiments are conducted with a water-based grafted copolymer that consists three monomers, poly(ethylene glycol)-grafted copolymers of N[3(dimethylamino)propyl]methacrylamide (DMAPMA) and acrylic acid (AA) mixture. (Hodaei et al. 2018). Mentioned superplasticizing polymer will be called as the copolymer from now on.

Our experiments showed us although α -Fe flakes are cleaned with ethanol after ball milling process, oleic acid residue remains on the surface of the flakes. Oleic acid coated particles are expected to show hydrophobic behavior with water-based solutions. While this property keeps α -Fe flakes dispersed in heptane and ethanol, and prevents oxidation of the flakes, it also displays incompatible behavior with the water-based copolymer. To inhibit incompatibility, α -Fe flakes are decided to be coated with another polymer, polyethylene glycol (PEG). There are PEG polymer varieties with different molecular weight. During our experiments, PEG with a molecular weight of 10.000 g/mol (PEG 10k) is being used.

To optimize the viscosity of the α -Fe suspension various ratios of PEG 10k, α -Fe flake, copolymer mixtures were tested. Our observations showed us that when copolymer to α -Fe flake ratio or PEG 10k to α -Fe flake ratio is increased, the tendency of the mixture to form a hydrogel is also increased. And when the polymer to flake ratio is decreased, printing capabilities are also decreased.

Previous research with the copolymer shows that 2% of the copolymer to particle ratio does have required consistency of ink mixture to be printed (Hodaei et al. 2018). However, the chain length of this copolymer is optimized for 50-100nm sized iron oxide nanoparticles. Even though our flakes are 100-200nm thick, the length of the particles are micron sized. To compensate size difference, copolymer to solid ratio is increased. Experiments with 2% and 9.5% copolymer to solid ratio did not show promising behavior. Successful printing tryouts ended up with 21% copolymer to solid ratio. PEG-10k to α -Fe flake ratio would be 1:1,34. The result is a printable ink with %65 solid content.

The first step of preparing polymer-based ink is coating flakes with PEG-10k. To prepare 20 grams of flake, 1,49 grams of PEG-10k is dissolved in water by using a magnetic stirrer and a fish. Then iron flakes are incorporated into the solution. In this step, it is not possible to use magnetic stirrer since iron is a ferromagnet. Hence PEG-10k-flake solution is mixed with a mechanical stirrer for half an hour. Excess water could be spilled out, and coated flakes should be dried. Enlarging surface increases the speed of evaporation, spreading flakes onto aluminum foil may speed up the evaporation process. Copolymer should be prepared in a beaker. The initial mixture of copolymer and flake suspension should have 40% solid content and 21% copolymer to solid ratio. While the initial copolymer solution is being mixed with a mechanical stirrer, PEG-10k coated iron flakes incorporated to the solution slowly. The suspension is left to be mixed with the stirrer and solid content is periodically checked. When the solid content is 65% suspension transferred into a syringe, ready to be printed. The mixing process does take as long as 36 hours. Since the evaporation rate of the water is not constant, there is no fixed time for this process.



Figure 9 Copolymer and iron flake suspension mixed with a mechanical stirrer

By the time of the 3D-printing experiments are operated, Fe_{16}N_2 phase was not available for our usage. Thus, instead of Fe_{16}N_2 flakes, $\alpha\text{-Fe}$ flakes are used. The SEM images shown in **Figure 18** demonstrate that $\alpha\text{-Fe}$ flakes exhibit the same particle shape and size with Fe_{16}N_2 flakes. It is expected to see no difference while printing Fe_{16}N_2 flakes.

2.2. Characterization

2.2.1. Vibrating Sample Magnetometer

Vibrating sample magnetometer (VSM) does take advantage of Faraday's law of induction. According to the law of induction, change of magnetic field in generates a change in the electric field. VSM does take small disk-shaped samples to measure the magnetic properties of it through manipulating the law of induction. VSM vibrates the magnetic sample in a space where surrounded by a sensing coil. The vibration of the magnetic sample causes a change in the magnetic field which creates eddy currents on the sensing coils. These currents are amplified with a lock-in amplifier and magnetic moment of the sample is given as output. To be able to measure the hysteresis behavior of the sample an electromagnet is being used. This electromagnet increases its magnetic field step by step, and in each step sensing coils report the measured magnetic. A basic schematic of a VSM system can be seen in **Figure 10** (Cullity and Graham 2008).

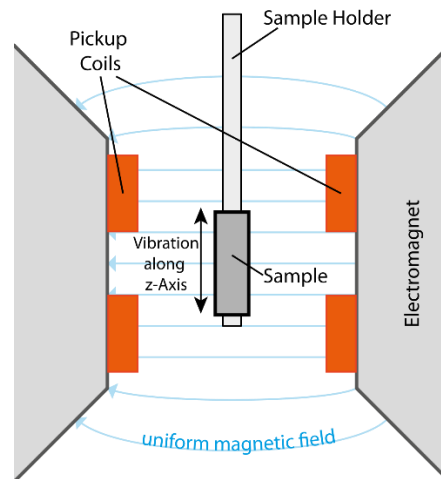


Figure 10 Representation of a VSM system

2.2.2. X-Ray Diffraction

Spatial arrangement is an important parameter for atoms as it strongly affects the magnetic, optical, mechanical, etc. properties of materials in their solid state. In nature atoms of a solid material can be in a state of order (as in crystals) or relative disorder (as in amorphous materials) and researchers use various tools to “see” this arrangement. Most ubiquitous among these tools is the X-ray diffraction, where a monochromatic beam of X-rays shine on a sample and exit after internal reflections. These reflections are recorded as a function of incident beam angle and intensity, giving us an idea about the structure of the material.



Figure 11 Bruker D2 Phaser

The wavelength of incident X-ray is on the order of several angstroms, which means it can be affected by features as small as an atomic nucleus. X-rays reflect off of crystalline “planes” which are the two-dimensional arrangement of atoms with the same distance between two of such planes and this distance is directly related to interatomic distance. An incident X-ray enters the crystal by making an angle θ with the crystalline plane of interest, reflects off of the plane elastically and exits the crystal at $180 - \theta$ angle. Considering a second X-ray to hit the same plane at a distance d away, there is a possibility that the extra distance traveled by this ray of light to be an integer multiple of the wavelength of this light. If this condition is met, constructive interference occurs and intensity is amplified, any other distance causes destructive interference and intensity

drops. When millions of such event occur in the crystal, a pattern emerges, and a strong reflection can be seen from the diffractogram. This reflection defines a relation between the interplanar distance for this crystal and with the help of other reflections, it gives us an idea about the geometry and structure of the material. This process can be summarized by Bragg's law of diffraction as;

$$n * \lambda = 2 d \sin(\theta)$$

where θ is the angle of incidence on the plane of diffraction, λ is the wavelength of X-ray, d is the interplanar distance and n is the integer number. The mechanism of action can be seen in **Figure 12** below.

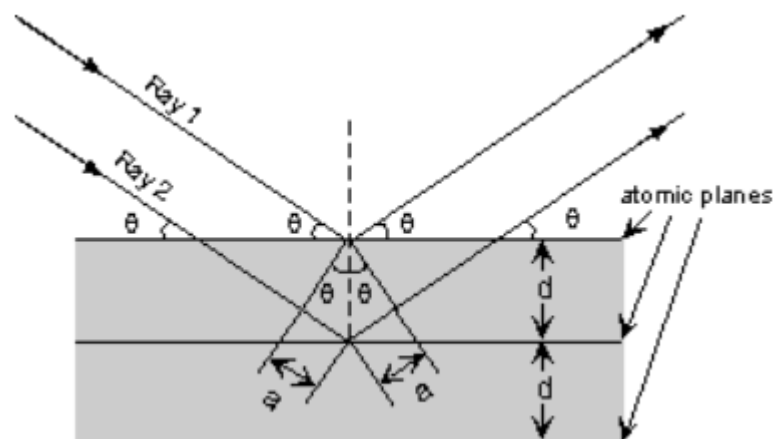


Figure 12 Bragg's law in action

2.2.3. Scanning Electron Microscopy

Scanning Electron Microscopy (SEM) is one of the most utilized equipments for materials research and has a resolution up to several nanometers, which sits between confocal (visible light) and Transmission Electron Microscopy (TEM). The equipment involves an electron generator, also known as an electron gun, a beam path within which electrons are focused on a narrow point via electromagnets (or magnetic lenses) and a

sample chamber which houses sample and all the detector windows. The whole system is under vacuum to prevent arcing and to provide a clear path for electrons.

The SEM utilized in this thesis (Leo SUPRA 35VP FEG-SEM, see **Figure 13**) is equipped with a field-emission gun, which can provide a higher flux of electrons and consequently a clearer and brighter image. After ejection, electrons pass through a number of condenser lenses that shrink the beam diameter. Unfortunately, there is a limit to this beam diameter since electrons are negatively charged and push each other back. The last lens in an SEM column is the condenser lens, which focuses the beam into a point with a diameter of several nanometers. An advantage of SEM compared to other microscopies is that it has a large depth of field, thanks to relatively low energy beam and non-optical image formation mechanism.

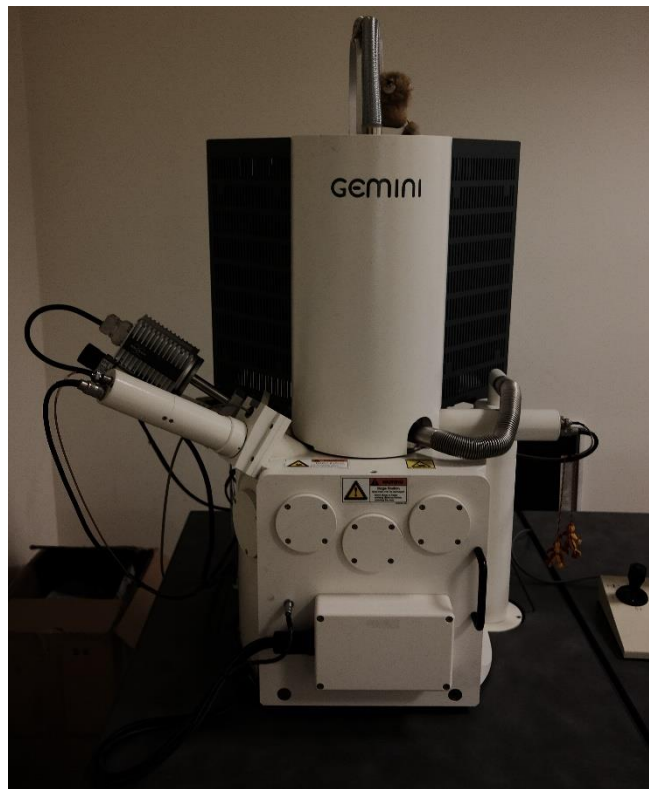


Figure 13 Leo SUPRA 35VP FEG-SEM

The scanning part of the system arises from several magnets positioned around the condenser lens that raster the beam on the region of interest. Any electron that is released from the sample after beam contact is collected at several detectors in the sample

chamber. The backscattered electron detector is positioned inside the condenser lens and can only pick up electrons that have inelastically scattered from atomic nuclei. These electrons, therefore, have Z-contrast (atomic weight) and can be utilized for phase differentiation. The secondary electrons are emitted from the sample in all directions and have much lower energy, which can be picked by a positively charged detector. The region from which secondary electrons emerge is called interaction volume and is a function of sample shape, voltage, and atomic mass. The interaction volume ultimately determines the resolving power of the SEM equipment. The teardrop shape from which electrons escape the sample can be seen in **Figure 14**.

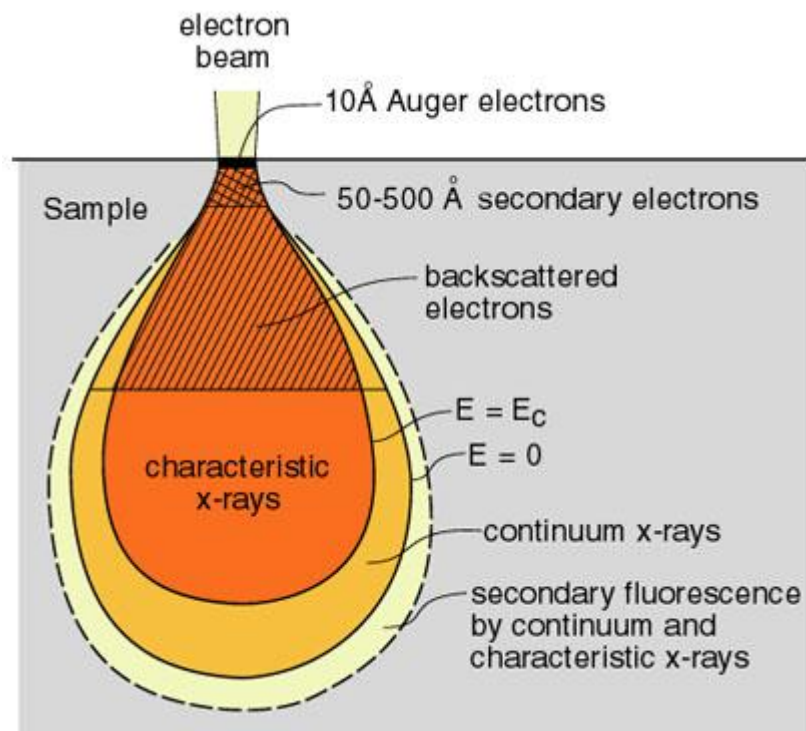


Figure 14 The teardrop shape of the interaction volume

3. RESULTS AND DISCUSSION

3.1. Particle Size Analysis

After the ball milling process, refined iron powder demonstrates two different structures. Black color of the heptane liquid implies that iron nanoparticles are emerged and appeared as a colloid in heptane, and iron flakes become the sediment of the suspension (slurry). Surfactant assisted ball milling process resulted in crushed powders turning into flakes and with the help of the oleic acid iron nanoparticles are dispersed in the heptane solvent and remained nano-sized. To analyze flake iron structures and iron nanoparticles, two different characterization method is required. DLS method is used to measure nanoparticle size, and SEM images are utilized to understand the size and shape of the iron flakes.

3.1.1. DLS Results

Ball milling experiments are conducted in three different rotation speed of the planetary system, 30 rpm, 40 rpm, 50 rpm. A sample is taken in each 4th hour for 24 hours to observe the change of particle size by the time.

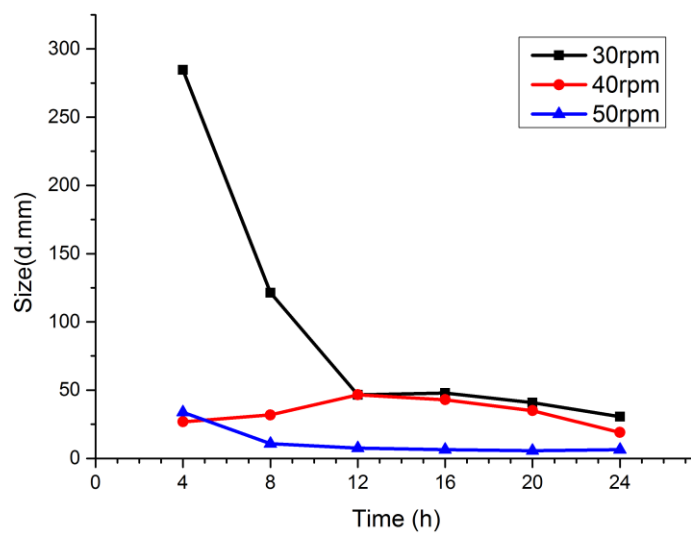


Figure 15 Particle Size vs Time graph

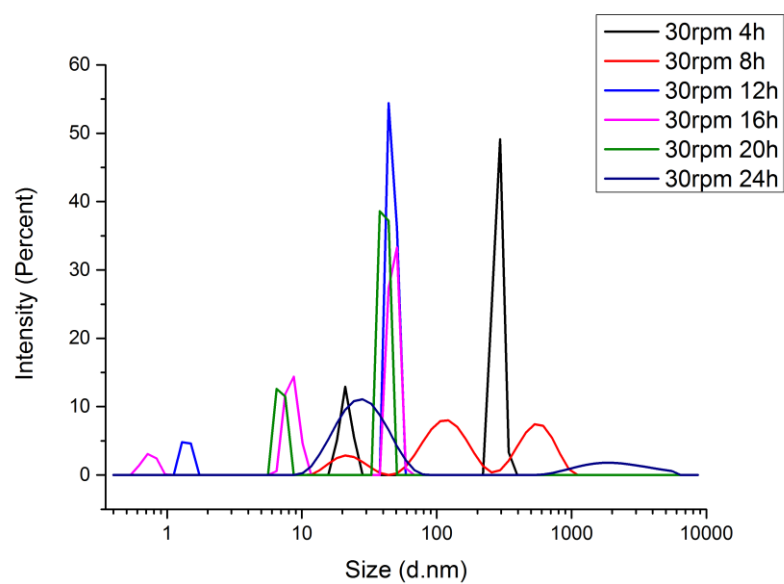


Figure 16 Size vs Intensity distribution of 30 rpm speed

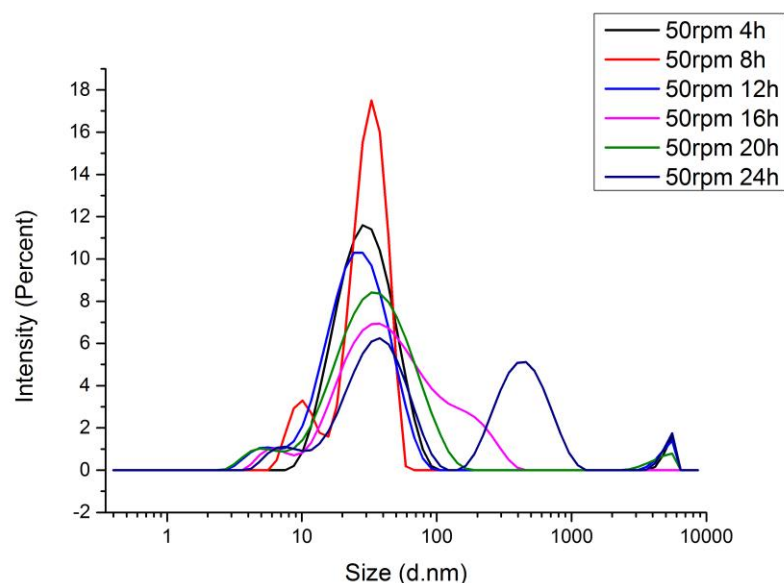


Figure 17 Size vs Intensity distribution of 50 rpm speed

Figure 15 shows that iron powder that is milled with 50 rpm speed achieves the smallest mean nanoparticle size. When **Figure 16** and **Figure 17** are compared, it can be seen that at 50 rpm particle size more consistent and at 30 rpm nanoparticles are more randomly sized. The ball milling process is driven by the mechanical energy transferred from steel balls to the powder to be milled. Mechanical energy depends on the weight of the balls and the rotation speed. **Figure 16** shows randomly sized pattern because the energy created by the 30-rpm speed is not enough to consistently reduce the size of the nano-particles. While rotating at 30-rpm, particles do break from the flakes; however particles may not reduce in size during the period of 4 hours. This is the reason for the random distribution in **Figure 16**, in each 4 hours period new particles breaks-up to the suspension with different sizes. It appears that at 50 rpm, these particles reduce in size more consistently because of the higher energy. For all DLS measurements, peaks appeared above 100nm corresponds to flakes in the solution Hence for the nitridation procedure, 20 grams of iron flake batch is prepared by milling for 24 hours at 50 rpm.

3.1.2. SEM Analysis of Flakes

Before starting the nitridation process, iron flakes are examined under SEM. Iron flakes are monitored before and after the nitridation process and SEM images are compared.

It is observed through SEM images in **Figure 18(c)** that thickness of the iron flakes is in the scale of 100 nm. Images do not show a sign of agglomeration. Before and after nitridation process Iron flakes show same morphology, thus preserves its flake shape.

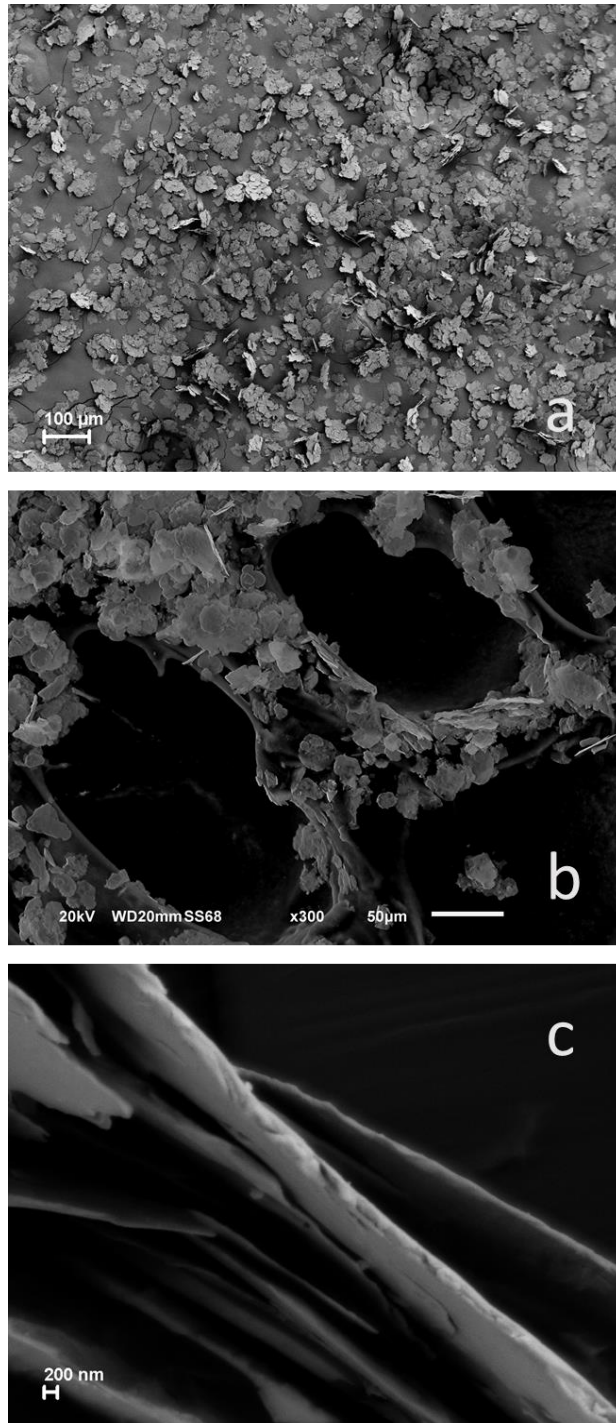


Figure 18 (a) shape and distribution of the Iron flakes, (b) after nitridation process (c)thickness of the iron flakes,

3.2. Phase Analysis

In this part of the thesis phase composition of the iron flakes will be examined. The workflow will start with showing characteristic peaks of possible phase structures. Results will be compared with α -Fe, Fe₂N, Fe₃N, and Fe₁₆N₂. Nitridation experiments are conducted with varying temperature, nitridation time. After several tryouts with different reduction times, it is seen that change in reduction time does not change the experiment results, thus reduction time is fixed to 2 hours. Phase stability, under air exposure and vacuum, is tested. As the last attempt to increase Fe₁₆N₂ phase transformation, the flakes are stirred in every 16 hours until nitridation time reaches 128 hours and the results of the measurements are given.

Composition analysis will be made through “PowderCell” application. PowderCell does composition calculations based on Rietveld refinement. This research is focused on the synthesis and 3D-printability, thus composition analysis is not detailed and considered just to give an idea about the efficiency of parameter changes. Since Rietveld analysis depends on fitting a reference curve onto the XRD graph, results are not always consistent. Moreover, after ball milling process XRD results of iron flakes show a textured behavior. Rietveld analysis with texture and background noise increases the complexity of the process and increases the inconsistency.

3.2.1. Simulated XRD Graphs

Here between **Figure 19** and **Figure 22** XRD simulations of α -Fe, Fe₂N, Fe₃N, and Fe₁₆N₂ can be seen. These are the simulated XRD data used during the composition analysis through PowderCell.

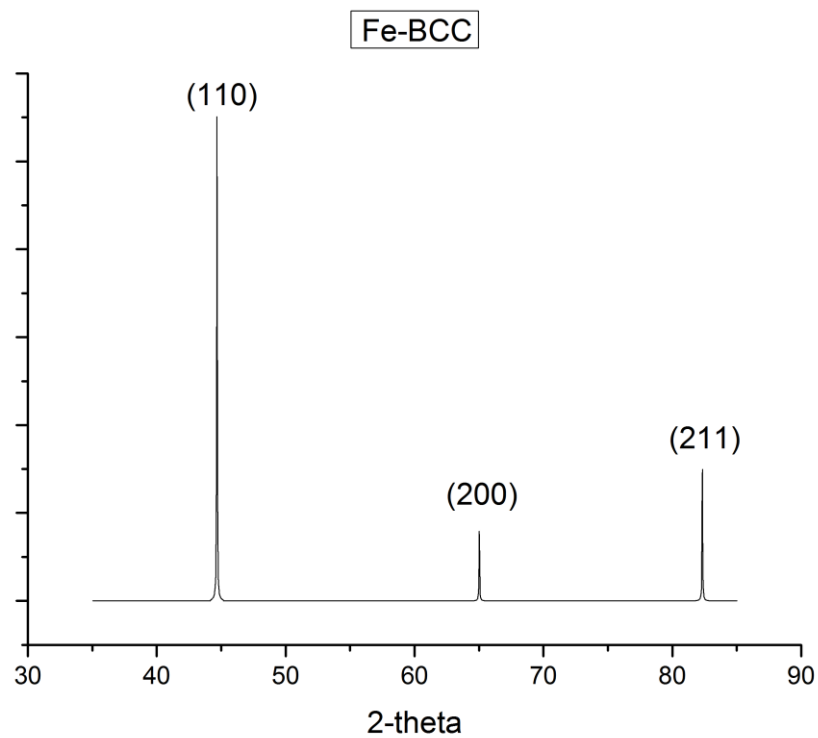


Figure 19 α -Fe simulated XRD peaks

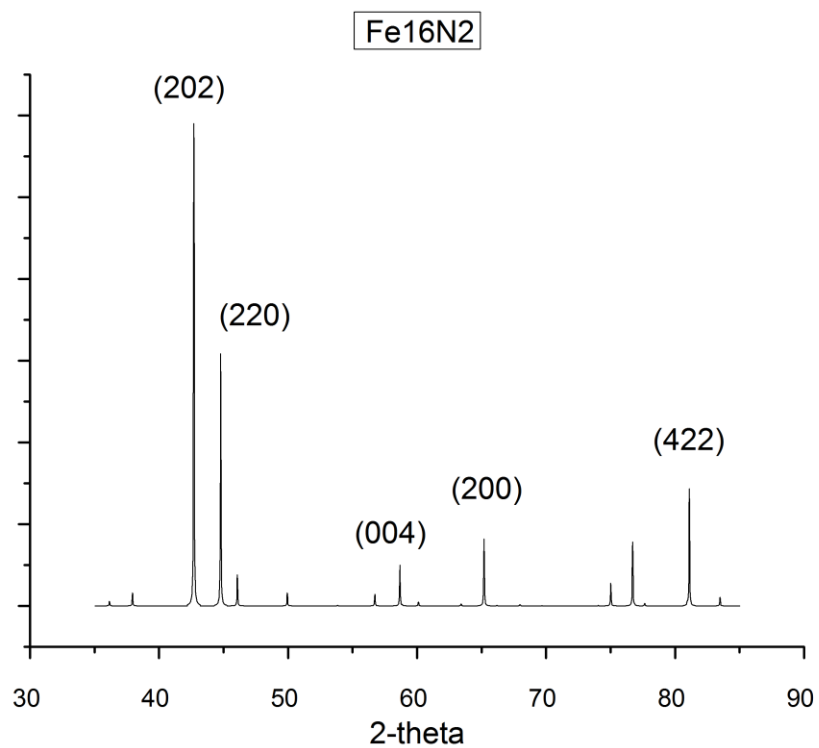


Figure 20 Fe₁₆N₂ simulated XRD peaks

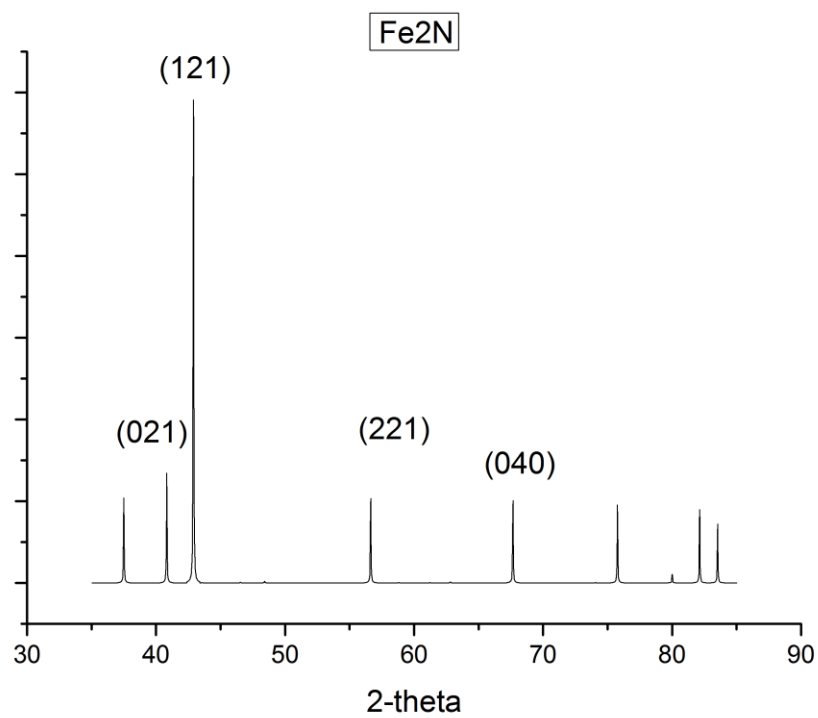


Figure 21 Fe₂N simulated XRD peaks

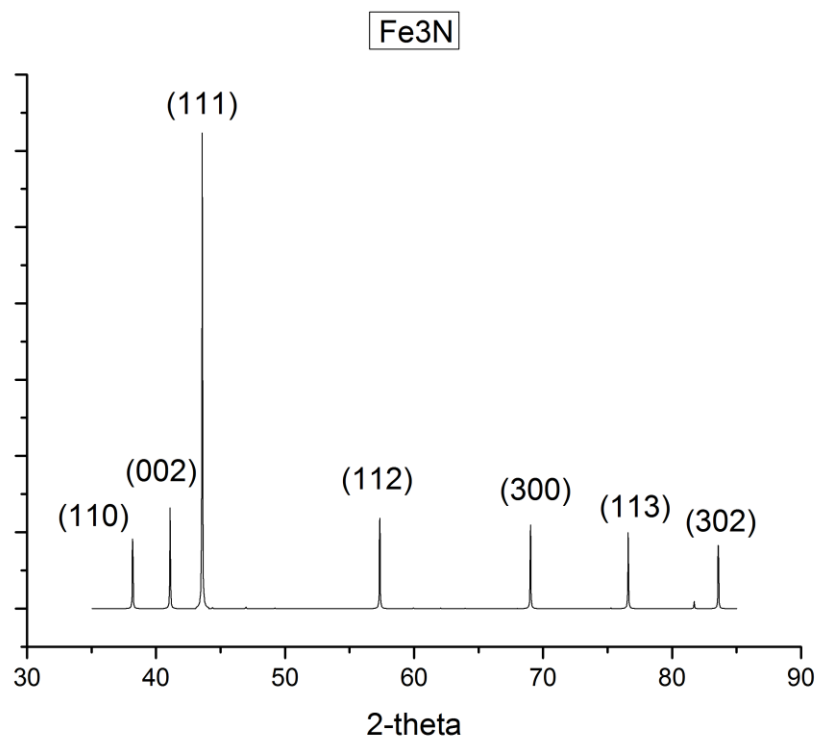


Figure 22 Fe₃N simulated XRD peaks

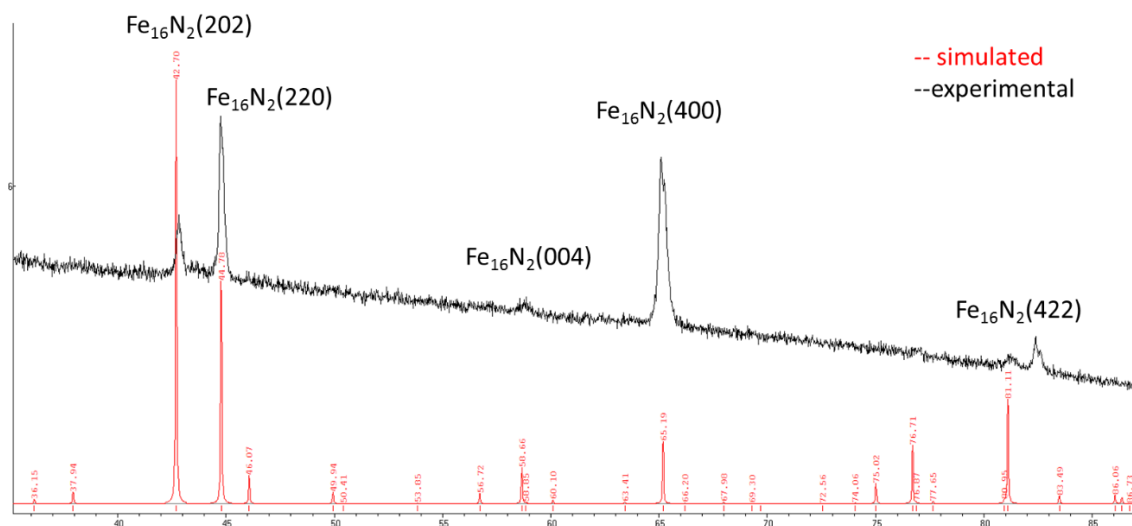


Figure 23 Comparison of XRD measurement of synthesized Fe_{16}N_2 flakes with simulated Fe_{16}N_2 XRD peaks

Figure 23 shows that strongest peaks of the simulated XRD graph of Fe_{16}N_2 match exactly to our experimental XRD graph. It should be noted that this composition also includes $\alpha\text{-Fe}$, thus it also consists strongest peaks of $\alpha\text{-Fe}$. Strongest peaks that belong to $\alpha\text{-Fe}$ is very similar to Fe_{16}N_2 , however, (202) and (422) peaks of Fe_{16}N_2 helps to separate it from $\alpha\text{-Fe}$ and other iron-nitride phases, Fe_2N and Fe_3N . The information given through the measurement data's will be discussed throughout the chapter.

3.2.2. XRD Results and Phase Composition

Here will be shown raw data of the significant XRD measurements to indicate the evaluation path of the graphs. Results of the analysis of the XRD measurements are given through the tables below. During the aforementioned first stages of the nitridation process, synthesis trials have resulted in either no phase conversion ($\alpha\text{-Fe}$) or conversion to other iron-nitride phases Fe_2N and Fe_3N . Brief explanation of the first stage trial would be as the following:

- 150 °C, under 50 scc/m N_2 gas flow, 1h to 24h: no phase transition

- 150 °C, under 50 scc/m to 200 scc/m NH₃ gas flow, 1h to 48h: no phase transition
- 300°C-400°C-500°C, under 50 scc/m NH₃ gas flow, 1h to 24h: 100% Fe to Fe₂N transition
- 400°C 1h → 170°C 14h, under 20scc/m NH₃ gas flow: 100% Fe to Fe₂N transition

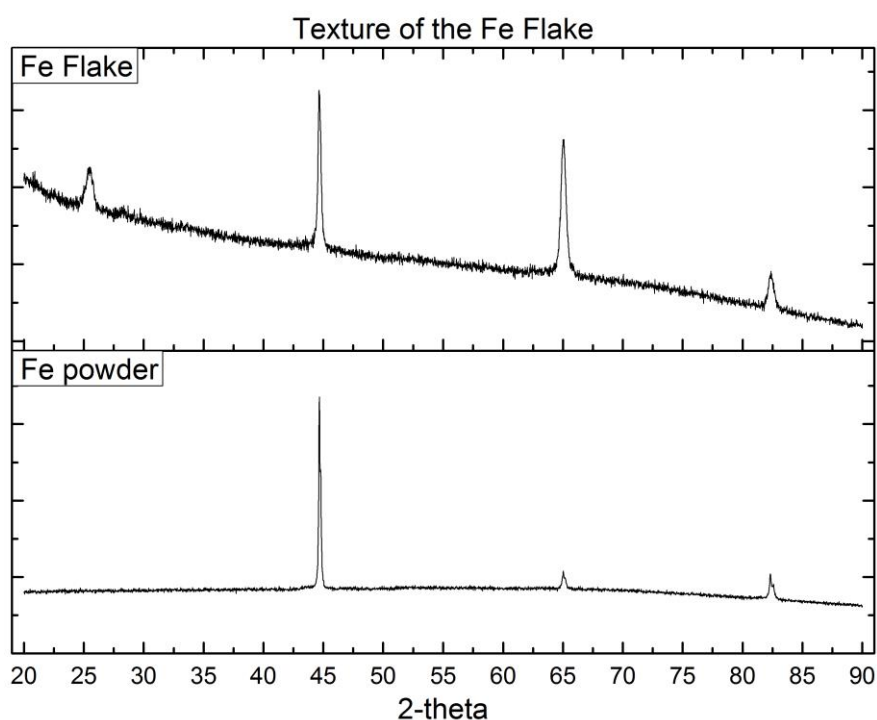


Figure 24 XRD comparison of Fe flake and Fe powder

Before going any further it should be stated that flakes are textured. As it can be seen in **Figure 19** α -Fe is expected smaller (200) peak, compared to the (110) peak. However, the XRD measurement of the α -Fe flake shows stronger (200) peak. It indicates that Fe flakes gained texture after the ball milling process. Thus, PowderCell composition analysis in the rest of this chapter is made with preferred orientation correction, considering the textured appearance of Fe flakes. Parameters for preferred orientation is set as “4%” on the “(200) plane” which acquired through PowderCell Rietveld analysis.

3.2.2.1. Nitridation Time and Temperature dependency of Fe₁₆N₂ composition

Table 2 Composition results of the PowderCell analysis for 16h nitridation with varying temperatures

16h	Fe₂N	Fe₃N	Fe₁₆N₂	α-Fe
150 °C	1,0%	0,8%	8,3%	89,9%
160 °C	0,4%	1,5%	19,4%	78,7%
170 °C	1,0%	4,5%	29,2%	66,3%
180 °C	0,2%	4,3%	40%	56,6%
190 °C	2,2%	7,7%	52,7%	37,4%
200 °C	10,8%	12,7%	25,3%	51,2%

According to data given in **Table 2**, Fe₁₆N₂ transition tendency increases with the increasing temperature. 190°C seems as the critical temperature in this table, phase transition becomes in the favor of the Fe₃N and Fe₂N beyond this point. It can be seen that at 200°C Fe₁₆N₂ ratio dropped drastically and Fe₂N ratio is increased. The experience came from the first stage of the experiments tells that higher temperature is more favorable for Fe₃N and Fe₂N transition. Besides 200°C is considerably closer to the decomposition temperature of the Fe₁₆N₂, 222°C. Thermodynamic approach also suggests that higher temperatures more favorable for other phases (see **Figure 2**).

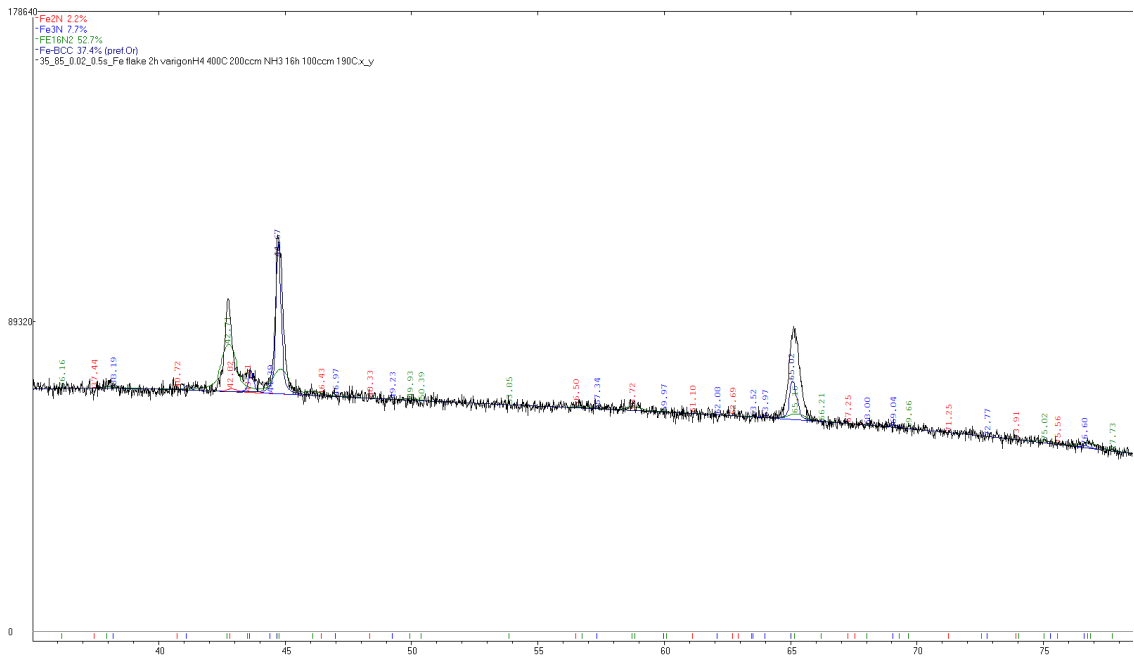


Figure 25 Rietveld analysis of Fe_{16}N_2 sample with highest transition (190°C 16h) through PowderCell

Table 3 Fe_{16}N_2 phase percentage calculations with PowderCell, an overview of the research

Temperature/Time (Fe_{16}N_2)	16h	40h	60h	80h	160h
150 °C	8,3%	-	-	-	-
160 °C	19,4%	-	35%	39,3%	34,7%
170 °C	29,2%	40,3%	18,8%	20,7%	-
180 °C	40%	-	-	-	-
190 °C	57,2%	28,6%	-	-	-
200 °C	25,3%	-	-	-	-

Table 3 shows the overview of synthesis tryouts briefly. Relation of the aimed phase transition and its dependency on temperature and nitridation time can be seen. This information demonstrates that Fe_{16}N_2 transition depends mostly on the nitridation temperature. Lower temperatures, such as 160°C requires more time to achieve the same percentage as higher temperatures. When this information is merged with **Table 6**, it can

be seen that increase in time does not always result in an increase in Fe₁₆N₂ transition. Fe₁₆N₂ transition reaches its saturation point on around 40% (excluding 190°C 16h samples) and does not show any more phase transition.

3.2.2.2. Stability of Fe₁₆N₂ flakes under vacuum and air exposure

Table 4 PowderCell analysis of the vacuum stored Fe₁₆N₂ (180 °C 16h)

180 °C 16h	Fe₂N	Fe₃N	Fe₁₆N₂	α-Fe
Fresh	0,2%	4,3%	40%	55%
5 days vacuum	0%	3,9%	29,8%	66,3%

Table 5 PowderCell analysis of the vacuum stored Fe₁₆N₂ (190 °C 16h)

190 °C 16h	Fe₂N	Fe₃N	Fe₁₆N₂	α-Fe
Fresh	2,2%	7,7%	52,7%	37,4%
40 days vacuum	3,3%	13,2%	54,3%	29,3%

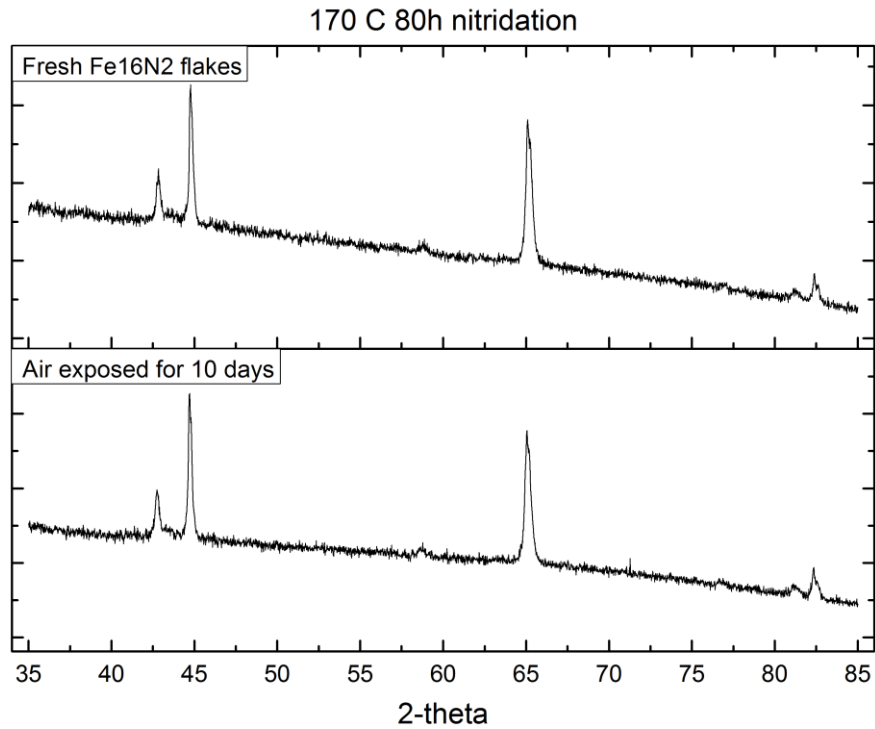


Figure 26 XRD comparison of fresh and air exposed Fe_{16}N_2 flakes

Figure 26 shows there is no change in peak intensities of the fresh and the air exposed sample. **Table 4** and **Table 5** do not show any difference out of the error margin of phase calculations. These results show that Fe_{16}N_2 flakes are stable under air exposure and vacuum and do not disintegrate.

3.2.2.3. Analysis of the effect of the stirring

In this set of experiment, the top and bottom of the crucible are mixed in every 16 hours, to understand whether there is a change in phase transformation percentage between the bottom and top of the sample. **Table 6** indicates there is no significant change in Fe_{16}N_2 transformation. It appears there is no difference between the top and the bottom of the sample.

Table 6 PowderCell analysis of the stirred samples

170 °C	Fe₂N	Fe₃N	Fe₁₆N₂	α-Fe
16h	0%	4,5%	29,2%	66,3%
32h	0%	3,5%	24,9%	71,6%
48h	0%	2,9%	27,4%	69,8%
64h	0%	4,6%	36,3%	59,1%
80h	0,9%	3,4%	32,7%	63%
96h	0%	4,3%	26,7%	69%
112h	0%	2,9%	31,4%	65,7%
128h	1,9%	5,1%	33,7%	59,3%
272h	0%	4,4%	34,3%	65,3%

3.3. Magnetic Properties

3.3.1. VSM Results

Samples with the highest Fe₁₆N₂ phase transformation are tested for the magnetic properties. Tests are conducted with a VSM setup. Synthesis parameters of the tested samples are as the following: 170°C 40h nitridation, 180°C 16h nitridation, 190 °C 16h nitridation, α-Fe no nitridation. 170°C 40h sample made out the highest coercivity and M_s values. Measurement results and comparison between α-Fe flakes can be seen below. **Figure 27** does show the magnetic moment and coercivity with an inlet. **Figure 28** and **Figure 29** are to compare coercivity and magnetic moment values of α-Fe and Fe₁₆N₂.

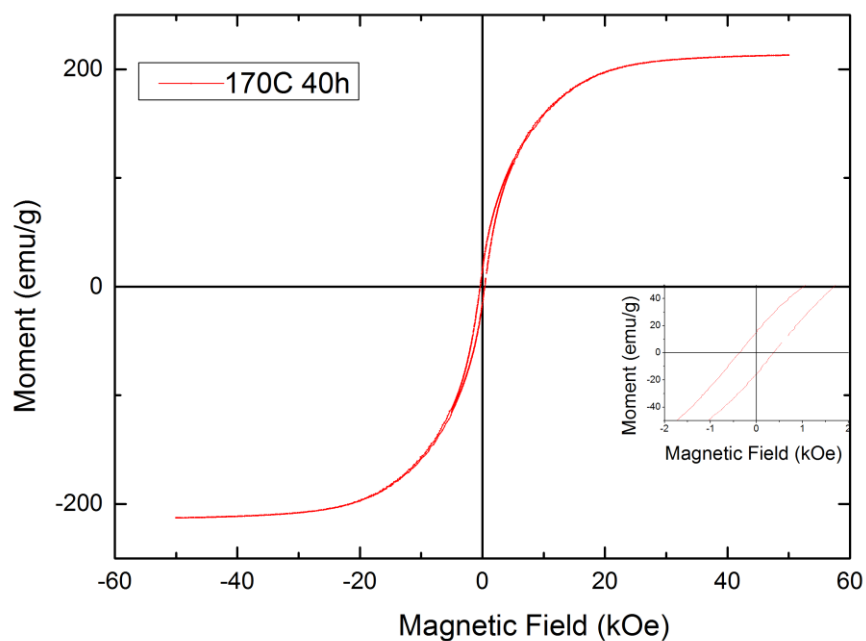


Figure 27 VSM measurement of Fe_{16}N_2 flake (nitridation for 40 hours at 170°C)

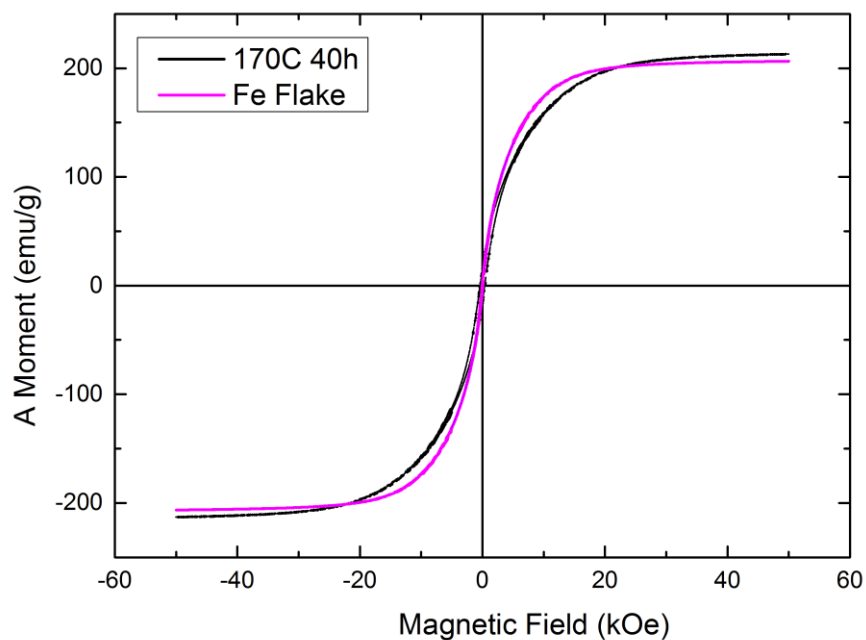


Figure 28 Comparison of Fe_{16}N_2 flake with Fe flake

In nature, iron does have the highest magnetic saturation. However low coercivity of iron makes it inconvenient to be used as magnet. As a result of the low coercivity, iron lose its magnetic polarity easily. Intrinsic anisotropy induced magnetic properties of Fe_{16}N_2 flakes exhibits higher M_s value and coercivity compared to the α -Fe flakes. According to our measurements, samples that contain high concentrations of Fe_{16}N_2 show higher magnetization and high room temperature coercivity of 367 Oe compared to 71 Oe for pure Fe flakes.

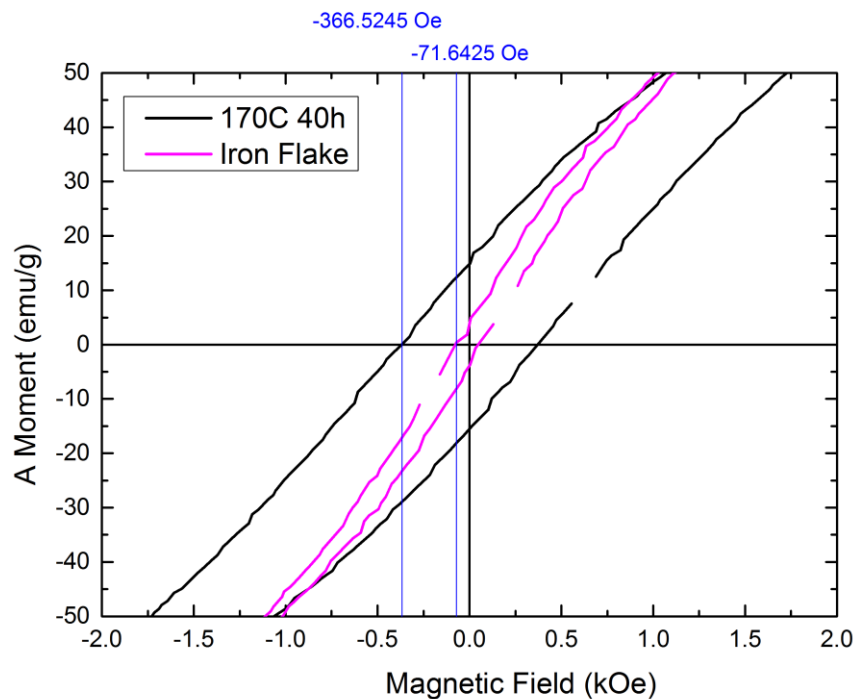


Figure 29 Enlarged VSM measurement data to show coercivity difference of Fe_{16}N_2 and Fe flakes

3.4. Printed Iron Structure

Sample in **Figure 30** is printed with our aforementioned copolymer, then sintered in a tube furnace for 24 hours at 900 °C under Argon gas flow, then structure is cut with diamond saw and smoothed with sandpaper (see **Figure 32**). Printing parameters of the sample shown in **Figure 30** is as the following :

- Iron ink solid content 65 wt%
- 40% fill rate
- 0.91mm nozzle diameter
- 10mm/sec

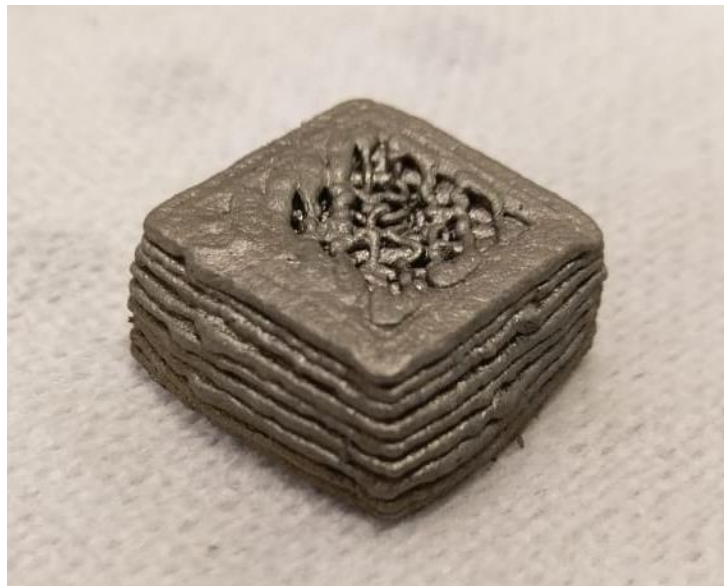


Figure 30 3D-printed iron flake sample

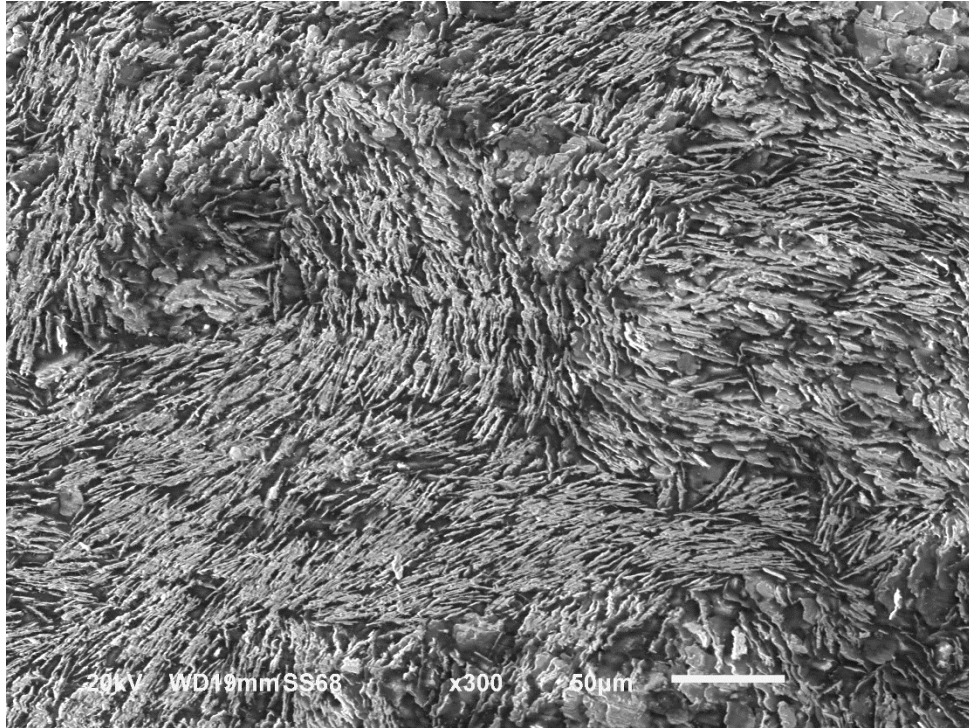


Figure 31 SEM image of iron flakes distribution in polymer

Iron flakes distribution and the morphology of the structure after sintering process are examined under SEM. It is important to mention here that since the prepared ink is soft without curing, UV curable photoresist, Su8, is used to keep flakes in order while cutting the structure with a diamond saw to see the cross section and examine the flake orientation. In **Figure 31** SEM image of iron flakes distribution in polymer **Figure 31** orientation of the flakes can be seen. Because of its flake structure, particles have tendency to stay in order. **Figure 32** shows after sintering process whole structure are unified.

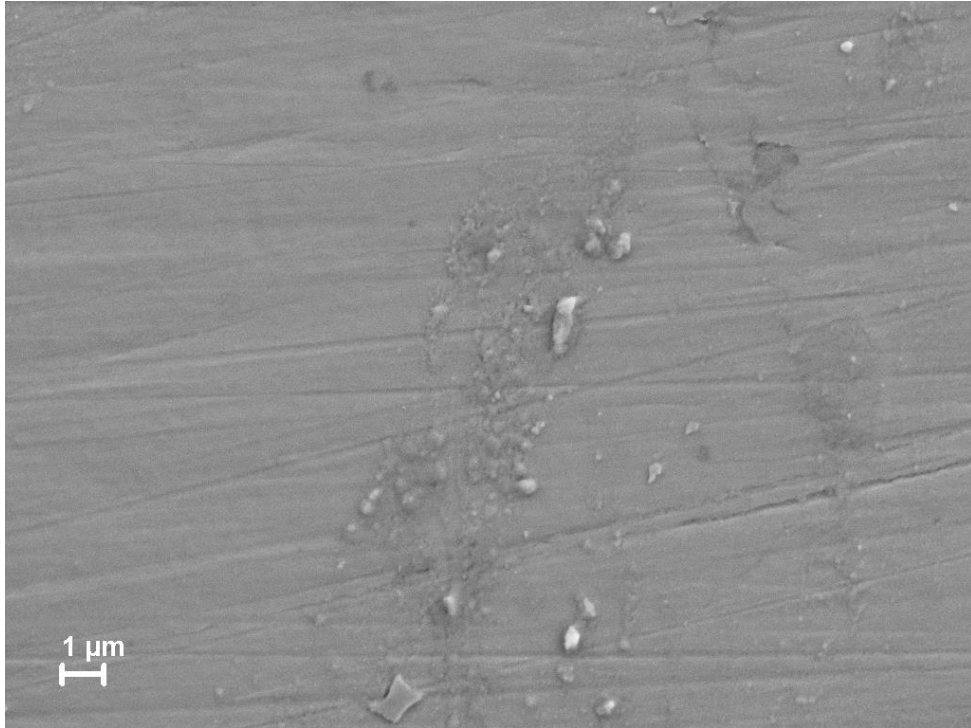


Figure 32 SEM image of the cross section of 3D printed iron flakes after sintering

3.5. Discussion and Future Work

A brief discussion about the overall process and remarks will be given here.

The nitridation process also applied on a silicon substrate coated with 50nm iron thin film. XRD measurement did not show any phase transition. Substrate-iron interference could be the reason for this. As mentioned in the first chapter, N atoms diffuse into BCC iron as interstitial atom, which results with size increment in cell parameters. Substrate-iron interference may inhibit iron cell parameters from increasing in size.

An observation about the composition calculations should be noted here. Because of the exaggerated (200) peak of the iron flake, Rietveld refinements are made with the texture orientation. However, when the same refinements made without entering texture information to the PowderCell, slightly different results are observed. Without texture information, Rietveld fittings have resulted with 50% - 57% of Fe_{16}N_2 transition most of

the time. Because of the exaggerated (200) peak, textured results are used. These calculations should be supported by TEM and XPS analysis. Accurate calculation of the volume ratio of Fe_{16}N_2 with XPS characterization is available in the literature (Jiang et al. 2015). Another factor here is the XRD measurement deviation caused by the XRD sample preparation error. The current setup produces around 100mg of Fe_{16}N_2 in each iteration. To be able to measure it, the sample is distributed on a double-sided sticker on a microscope glass. It is not an ideal way of measurement, thus should be supported with TEM characterization as future work.

Current results do not give any information about the local phase transition kinetics of Fe_{16}N_2 . It is unknown whether some of the flakes encounters total phase transition or not. Depth profile XPS analysis could give information about phase transition kinetics. Moreover, the edge of the nitridated iron flakes could be examined with high-resolution TEM, in order to understand how and where happens the phase transition. A crystallographic examination could also help.

To increase the 3D-printable ink quality, rheology measurements could be done as future work. Chain length optimization of the copolymer could also increase the solid content of the ink. Zeta potential of the iron particles could be quantified to be able to prepare more compatible polymer.

4. CONCLUSION

A novel procedure to synthesize Fe_{16}N_2 phase is optimized during this research. Tube furnace system and gas flow setup established for the nitridation process. Handmade Molybdenum crucibles are made to prevent contamination between Fe_{16}N_2 batches. Ball milling parameters are swept, and output is analyzed by DLS characterization. A successful Fe_{16}N_2 phase transition is observed through XRD. This research was aimed to increase magnetic properties of Iron, VSM measurements show that magnetic moment and coercivity of the synthesized samples are increased compared to the iron flakes. Polymer based iron ink was optimized for 3D-printing, and a structure is printed as a proof of concept.

This research appears as a first step to suggest a synthesis method that could scale up the Fe_{16}N_2 production. With mentioned future work appended, this research could pave the way to offer a cost-efficient and environment-friendly magnet alternative to the energy industry.

BIBLIOGRAPHY

- Abdellateef, M.A., C. Heiden, H. Lemke, F.M. El-Hossary, and K. Baerner. 2003. "Magnetic Properties and Structure of the A"-Fe₁₆N₂ Films." *Journal of Magnetism and Magnetic Materials* 256 (1–3): 214–20.
[https://doi.org/10.1016/S0304-8853\(02\)00479-1](https://doi.org/10.1016/S0304-8853(02)00479-1).
- Abdelrahman, Ahmed S., and Mohamed Z. Youssef. 2017. "A Cost Effective Magnetic/Electronic Design for the Water Pump Application Drive: Analysis, Design, and Experimentation." In *Conference Proceedings - IEEE Applied Power Electronics Conference and Exposition - APEC*, 2329–35.
<https://doi.org/10.1109/APEC.2017.7931025>.
- Akdogan, Nilay G., George C. Hadjipanayis, and David J. Sellmyer. 2010. "Novel Nd₂Fe₁₄B Nanoflakes and Nanoparticles for the Development of High Energy Nanocomposite Magnets." *Nanotechnology* 21 (29): 295705.
<https://doi.org/10.1088/0957-4484/21/29/295705>.
- Akdogan, Nilay Gunduz. 2012. "Rare-Earth 3d Transition Metal Nanoparticles and Nanoflakes by Surfactant-Assisted High-Energy Ball Milling." University of Delaware.
- Alonso, Elisa, Andrew M. Sherman, Timothy J. Wallington, Mark P. Everson, Frank R. Field, Richard Roth, and Randolph E. Kirchain. 2012. "Evaluating Rare Earth Element Availability: A Case with Revolutionary Demand from Clean Technologies." *Environmental Science and Technology* 46 (6): 3406–14.
<https://doi.org/10.1021/es203518d>.
- Bell, David A, Brian F Towler, and Maohong Fan. 2011. "Ammonia and Derivatives." In *Coal Gasification and Its Applications*, 341–52. Elsevier.
<https://doi.org/10.1016/B978-0-8155-2049-8.10011-7>.
- Brown, David, Bao-Min Ma, and Zhongmin Chen. 2002. "Developments in the Processing and Properties of NdFeb-Type Permanent Magnets." *Journal of Magnetism and Magnetic Materials* 248 (3): 432–40.
[https://doi.org/10.1016/S0304-8853\(02\)00334-7](https://doi.org/10.1016/S0304-8853(02)00334-7).
- Byrneumledu, Charles Byrne Charles. 2012. "A Brief History of Electromagnetism Are We There Yet ?" <http://faculty.uml.edu/cbyrne/cbyrne.html>.

- Chin, Z.-H., and T.P. Perng. 1996. "Amorphization of Ni-Si-C Ternary Alloy Powder by Mechanical Alloying." *Materials Science Forum* 235–238 (October): 121–26. <https://doi.org/10.4028/www.scientific.net/MSF.235-238.121>.
- Cullity, B. D., and C. D. Graham. 2008. *Introduction to Magnetic Materials. The British Journal of Psychiatry*. Vol. 112. Hoboken, NJ, USA: John Wiley & Sons, Inc. <https://doi.org/10.1002/9780470386323>.
- Dirba, Imants. 2017. "Fe₈N_x Thin Films and Nanoparticles : From Intrinsic Properties Towards Magnetic Applications." Technische Universität Darmstadt.
- Du, Xiaoyue, and T. E. Graedel. 2011. "Global Rare Earth In-Use Stocks in NdFeB Permanent Magnets." *Journal of Industrial Ecology* 15 (6): 836–43. <https://doi.org/10.1111/j.1530-9290.2011.00362.x>.
- Dulbecco, R. 1954. "PLAQUE FORMATION AND ISOLATION OF PURE LINES WITH POLIOMYELITIS VIRUSES." *Journal of Experimental Medicine* 99 (2): 167–82. <https://doi.org/10.1084/jem.99.2.167>.
- Edwards, P. P., V. L. Kuznetsov, W. I F David, and N. P. Brandon. 2008. "Hydrogen and Fuel Cells: Towards a Sustainable Energy Future." *Energy Policy* 36 (12): 4356–62. <https://doi.org/10.1016/j.enpol.2008.09.036>.
- Feng, L, D Zhang, F Wang, L Dong, S Chen, J Liu, and X Hui. 2017. "A New Structure of the Environment-Friendly Material Fe₁₆N₂." *Chemical Engineering Transactions* 61: 1501–6. <https://doi.org/10.3303/CET1761248>.
- Gölden, Dominik. 2018. "Magnetokristalline Anisotropie von Eisen-Dünnschichten Mit Interstitiellem Stickstoff Und Bor." Technische Universität Darmstadt.
- Gutfleisch, Oliver, Matthew A. Willard, Ekkes Brück, Christina H. Chen, S. G. Sankar, and J. Ping Liu. 2011. "Magnetic Materials and Devices for the 21st Century: Stronger, Lighter, and More Energy Efficient." *Advanced Materials* 23 (7): 821–42. <https://doi.org/10.1002/adma.201002180>.
- Gwenzi, Willis, Lynda Mangori, Concilia Danha, Nhamo Chaukura, Nothando Dunjana, and Edmond Sanganyado. 2018. "Sources, Behaviour, and Environmental and Human Health Risks of High-Technology Rare Earth Elements as Emerging Contaminants." *Science of the Total Environment*.

- <https://doi.org/10.1016/j.scitotenv.2018.04.235>.
- Haque, Nawshad, Anthony Hughes, Seng Lim, and Chris Vernon. 2014. "Rare Earth Elements: Overview of Mining, Mineralogy, Uses, Sustainability and Environmental Impact." *Resources* 3 (4): 614–35.
<https://doi.org/10.3390/resources3040614>.
- Hodaiei, Amin, Omid Akhlaghi, Navid Khani, Tunahan Aytas, Dilek Sezer, Buse Tatli, Yusuf Z. Menciloglu, Bahattin Koc, and Ozge Akbulut. 2018. "Single Additive Enables 3D Printing of Highly Loaded Iron Oxide Suspensions." *ACS Applied Materials and Interfaces* 10 (11): 9873–81.
<https://doi.org/10.1021/acsami.8b00551>.
- Ibeh, Chimaobi. 2018. "Analysis of 3D Printed NDFeB Polymer Bonded and Organic Based Magnets." *Theses*. New Jersey Institute of Technology.
<https://digitalcommons.njit.edu/theses/1634>.
- Jaćimović, Jaćim, Federico Binda, Lorenz G. Herrmann, Felix Greuter, Jessica Genta, Micha Calvo, Tomaž Tomše, and Reinhard A. Simon. 2017. "Net Shape 3D Printed NdFeB Permanent Magnet ." *Advanced Engineering Materials* 19 (8): 1700098. <https://doi.org/10.1002/adem.201700098>.
- Jack, D.H., and K.H. Jack. 1973. "Invited Review: Carbides and Nitrides in Steel." *Materials Science and Engineering* 11 (1): 1–27. [https://doi.org/10.1016/0025-5416\(73\)90055-4](https://doi.org/10.1016/0025-5416(73)90055-4).
- Ji, Nian, Valeria Lauter, Xiaowei Zhang, Hailemariam Ambaye, and Jian Ping Wang. 2013. "Strain Induced Giant Magnetism in Epitaxial Fe₁₆N₂ Thin Film." *Applied Physics Letters* 102 (7): 2–6. <https://doi.org/10.1063/1.4792706>.
- Jiang, Yanfeng, Jinming Liu, Pranav K. Suri, Greg Kennedy, Naresh N. Thadhani, David J. Flannigan, and Jian-Ping Wang. 2016. "Preparation of an A"-Fe₁₆N₂ Magnet via a Ball Milling and Shock Compaction Approach." *Advanced Engineering Materials* 18 (6): 1009–16. <https://doi.org/10.1002/adem.201500455>.
- Jiang, Yanfeng, Xiaowei Zhang, Aminul Al Mehedi, Meiyin Yang, and Jian-Ping Wang. 2015. "A Method to Evaluate α "-Fe₁₆N₂ Volume Ratio in FeN Bulk Material by XPS." *Materials Research Express* 2 (11): 116103.
<https://doi.org/10.1088/2053-1591/2/11/116103>.

- Jiles, David. 1991. *Introduction to Magnetism and Magnetic Materials*. First edit. Boston, MA: Springer US. <https://doi.org/10.1007/978-1-4615-3868-4>.
- Kartikowati, Christina Wahyu. 2018. "Preparation and Evaluation of Magnetic Nanocomposite Films and Fibers Containing α -Fe₁₆N₂ Nanoparticles." Hiroshima University.
- Kim, T. K., and M. Takahashi. 1972. "New Magnetic Material Having Ultrahigh Magnetic Moment." *Applied Physics Letters* 20 (12): 492–94. <https://doi.org/10.1063/1.1654030>.
- Kis-Varga, Miklos, and Dezső L. Beke. 1996. "Phase Transitions in Cu-Sb Systems Induced by Ball Milling." *Materials Science Forum* 225–227 (July): 465–70. <https://doi.org/10.4028/www.scientific.net/MSF.225-227.465>.
- Kita, Eiji, Kenichi Shibata, Yuji Sasaki, Mikio Kishimoto, and Hideto Yanagihara. 2017. "Magnetic Anisotropy in Spherical Fe₁₆N₂ Core-Shell Nanoparticles Determined by Torque Measurements." *AIP Advances* 7 (5): 2–7. <https://doi.org/10.1063/1.4974276>.
- Ma, B. M., J. W. Herchenroeder, B. Smith, M. Suda, D. Brown, and Z. Chen. 2002. "Recent Development in Bonded NdFeB Magnets." *Journal of Magnetism and Magnetic Materials* 239 (1–3): 418–23. [https://doi.org/10.1016/S0304-8853\(01\)00609-6](https://doi.org/10.1016/S0304-8853(01)00609-6).
- Mills, Allan A. 2004. "The Lodestone: History, Physics, and Formation." *Annals of Science* 61 (3): 273–319. <https://doi.org/10.1080/00033790310001642812>.
- Moradifar, P. 2015. "Microstructure Evaluation of Iron Nitride Interstitial Compound, as A Candidate for Permanent Magnetic Material." CASE WESTERN RESERVE UNIVERSITY.
- Mornet, Stéphane, Sébastien Vasseur, Fabien Grasset, and Etienne Duguet. 2004. "Magnetic Nanoparticle Design for Medical Diagnosis and Therapy." *Journal of Materials Chemistry* 14 (14): 2161–75. <https://doi.org/10.1039/b402025a>.
- Ogawa, Tomoyuki, Yasunobu Ogata, Ruwan Gallage, Naoya Kobayashi, Naoaki Hayashi, Yoshihiro Kusano, Shinpei Yamamoto, et al. 2013. "Challenge to the Synthesis of α -Fe₁₆N₂ compound Nanoparticle with High Saturation

- Magnetization for Rare Earth Free New Permanent Magnetic Material.” *Applied Physics Express* 6 (7): 073007. <https://doi.org/10.7567/APEX.6.073007>.
- Pepperhoff, Werner, and Mehmet Acet. 2001. *Constitution and Magnetism of Iron and Its Alloys. Synchrotron Radiation News*. Vol. 30. Engineering Materials. Berlin, Heidelberg: Springer Berlin Heidelberg. <https://doi.org/10.1007/978-3-662-04345-5>.
- Popov, Vladimir, Andrey Koptyug, Iliya Radulov, Fernando Maccari, and Gary Muller. 2018. “Prospects of Additive Manufacturing of Rare-Earth and Non-Rare-Earth Permanent Magnets.” *Procedia Manufacturing* 21 (March): 100–108. <https://doi.org/10.1016/j.promfg.2018.02.199>.
- Sakuma, Akimasa. 2002. “Electronic and Magnetic Structure of Iron Nitride, Fe₁₆N₂ (Invited).” *Journal of Applied Physics* 79 (8): 5570. <https://doi.org/10.1063/1.362245>.
- Sugita, Y., K. Mitsuoka, M. Komuro, H. Hoshiya, Y. Kozono, and M. Hanazono. 1991. “Giant Magnetic Moment and Other Magnetic Properties of Epitaxially Grown Fe₁₆N₂ Single-crystal Films (Invited).” *Journal of Applied Physics* 70 (10): 5977–82. <https://doi.org/10.1063/1.350067>.
- Sugita, Yutaka, Hiromasa Takahashi, Matahiro Komuro, Masukazu Igarashi, Ryo Imura, and Takashi Kambe. 1996. “Magnetic and Electrical Properties of Single-Phase, Single-Crystal Fe₁₆N₂ Films Epitaxially Grown by Molecular Beam Epitaxy (Invited).” *Journal of Applied Physics* 79 (8): 5576. <https://doi.org/10.1063/1.362246>.
- Suryanarayana, Cury. 2001. “Mechanical Alloying and Milling.” *Progress in Materials Science* 46 (1–2): 1–184. [https://doi.org/10.1016/S0079-6425\(99\)00010-9](https://doi.org/10.1016/S0079-6425(99)00010-9).
- Takagi, Kenta, Misaho Akada, Kimihiro Ozaki, Naoya Kobayashi, Tomoyuki Ogawa, Yasunobu Ogata, and Migaku Takahashi. 2014. “High-Pressure Sintering Behavior of A⁰-Fe₁₆N₂ Nanopowder.” *Journal of Applied Physics* 115 (10). <https://doi.org/10.1063/1.4868295>.
- Takahashi, H., K. Mitsuoka, M. Komuro, and Y. Sugita. 1993. “Ferromagnetic Resonance Studies of Fe₁₆N₂ Films with a Giant Magnetic Moment.” *Journal of Applied Physics* 73 (10): 6060–62. <https://doi.org/10.1063/1.353469>.

- Takahashi, H, M Igarashi, A Kaneko, H Miyajima, and Y. Sugita. 1999. "Perpendicular Uniaxial Magnetic Anisotropy of Fe₁₆N₂[001] Single Crystal Films Grown by Molecular Beam Epitaxy." *IEEE Transactions on Magnetics* 35 (5): 2982–84. <https://doi.org/10.1109/20.801054>.
- Weber, T., L. de Wit, F.W. Saris, and P. Schaaf. 1996. "Search for Giant Magnetic Moments in Ion-Beam-Synthesized A"-Fe₁₆N₂." *Thin Solid Films* 279 (1–2): 216–20. [https://doi.org/10.1016/0040-6090\(95\)08176-3](https://doi.org/10.1016/0040-6090(95)08176-3).
- Weiss, Burghard. 2000. "Selected Scientific Works of Hans Christian Ørsted. Translated and Edited by Karen Jelved, Andrew D. Jackson and Ole Knudsen. With an Introduction by Andrew Wilson. Princeton: Princeton University Press 1998. 647 Seiten. US\$ 90." *Berichte Zur Wissenschaftsgeschichte* 23 (1): 58–59. <https://doi.org/10.1002/bewi.20000230112>.
- Widenmeyer, Marc, Thomas C. Hansen, and Rainer Niewa. 2013. "Formation and Decomposition of Metastable A"-Fe₁₆N₂ from in Situ Powder Neutron Diffraction and Thermal Analysis." *Zeitschrift Fur Anorganische Und Allgemeine Chemie* 639 (15): 2851–59. <https://doi.org/10.1002/zaac.201300379>.
- Williams, Gerald, and Venkat Pattabathula. 2013. "One Hundred Years of Ammonia Production-A Recap of Significant Contributions to Feeding the World." In . American Institute of Chemical Engineers.
- Yang, Yongxiang, Allan Walton, Richard Sheridan, Konrad Güth, Roland Gauß, Oliver Gutfleisch, Matthias Buchert, et al. 2017. "REE Recovery from End-of-Life NdFeB Permanent Magnet Scrap: A Critical Review." *Journal of Sustainable Metallurgy* 3 (1): 122–49. <https://doi.org/10.1007/s40831-016-0090-4>.